

Measurements of the semileptonic decays $\bar{B} \rightarrow D\ell\bar{\nu}$ and $\bar{B} \rightarrow D^*\ell\bar{\nu}$ using a global fit to $DX\ell\bar{\nu}$ final states

B. Aubert,¹ M. Bona,¹ Y. Karyotakis,¹ J. P. Lees,¹ V. Poireau,¹ E. Prencipe,¹ X. Prudent,¹ V. Tisserand,¹ J. Garra Tico,² E. Grauges,² L. Lopez,^{3a,3b} A. Palano,^{3a,3b} M. Pappagallo,^{3a,3b} G. Eigen,⁴ B. Stugu,⁴ L. Sun,⁴ G. S. Abrams,⁵ M. Battaglia,⁵ D. N. Brown,⁵ R. N. Cahn,⁵ R. G. Jacobsen,⁵ L. T. Kerth,⁵ Yu. G. Kolomensky,⁵ G. Lynch,⁵ I. L. Osipenkov,⁵ M. T. Ronan,^{5,*} K. Tackmann,⁵ T. Tanabe,⁵ C. M. Hawkes,⁶ N. Soni,⁶ A. T. Watson,⁶ H. Koch,⁷ T. Schroeder,⁷ D. Walker,⁸ D. J. Asgeirsson,⁹ B. G. Fulsom,⁹ C. Hearty,⁹ T. S. Mattison,⁹ J. A. McKenna,⁹ M. Barrett,¹⁰ A. Khan,¹⁰ V. E. Blinov,¹¹ A. D. Bukin,¹¹ A. R. Buzykaev,¹¹ V. P. Druzhinin,¹¹ V. B. Golubev,¹¹ A. P. Onuchin,¹¹ S. I. Serednyakov,¹¹ Yu. I. Skovpen,¹¹ E. P. Solodov,¹¹ K. Yu. Todyshev,¹¹ M. Bondioli,¹² S. Curry,¹² I. Eschrich,¹² D. Kirkby,¹² A. J. Lankford,¹² P. Lund,¹² M. Mandelkern,¹² E. C. Martin,¹² D. P. Stoker,¹² S. Abachi,¹³ C. Buchanan,¹³ J. W. Gary,¹⁴ F. Liu,¹⁴ O. Long,¹⁴ B. C. Shen,^{14,*} G. M. Vitug,¹⁴ Z. Yasin,¹⁴ L. Zhang,¹⁴ V. Sharma,¹⁵ C. Campagnari,¹⁶ T. M. Hong,¹⁶ D. Kovalskiy,¹⁶ M. A. Mazur,¹⁶ J. D. Richman,¹⁶ T. W. Beck,¹⁷ A. M. Eisner,¹⁷ C. J. Flacco,¹⁷ C. A. Heusch,¹⁷ J. Kroseberg,¹⁷ W. S. Lockman,¹⁷ T. Schalk,¹⁷ B. A. Schumm,¹⁷ A. Seiden,¹⁷ L. Wang,¹⁷ M. G. Wilson,¹⁷ L. O. Winstrom,¹⁷ C. H. Cheng,¹⁸ D. A. Doll,¹⁸ B. Echenard,¹⁸ F. Fang,¹⁸ D. G. Hitlin,¹⁸ I. Narsky,¹⁸ T. Piatenko,¹⁸ F. C. Porter,¹⁸ R. Andreassen,¹⁹ G. Mancinelli,¹⁹ B. T. Meadows,¹⁹ K. Mishra,¹⁹ M. D. Sokoloff,¹⁹ P. C. Bloom,²⁰ W. T. Ford,²⁰ A. Gaz,²⁰ J. F. Hirschauer,²⁰ M. Nagel,²⁰ U. Nauenberg,²⁰ J. G. Smith,²⁰ K. A. Ulmer,²⁰ S. R. Wagner,²⁰ R. Ayad,^{21,†} A. Soffer,^{21,‡} W. H. Toki,²¹ R. J. Wilson,²¹ D. D. Altenburg,²² E. Feltresi,²² A. Hauke,²² H. Jasper,²² M. Karbach,²² J. Merkel,²² A. Petzold,²² B. Spaan,²² K. Wacker,²² M. J. Kobel,²³ W. F. Mader,²³ R. Nogowski,²³ K. R. Schubert,²³ R. Schwierz,²³ J. E. Sundermann,²³ A. Volk,²³ D. Bernard,²⁴ G. R. Bonneaud,²⁴ E. Latour,²⁴ Ch. Thiebaux,²⁴ M. Verderi,²⁴ P. J. Clark,²⁵ W. Gradl,²⁵ S. Playfer,²⁵ J. E. Watson,²⁵ M. Andreotti,^{26a,26b} D. Bettoni,^{26a} C. Bozzi,^{26a} R. Calabrese,^{26a,26b} A. Cecchi,^{26a,26b} G. Cibinetto,^{26a,26b} P. Franchini,^{26a,26b} E. Luppi,^{26a,26b} M. Negrini,^{26a,26b} A. Petrella,^{26a,26b} L. Piemontese,^{26a} V. Santoro,^{26a,26b} R. Baldini-Ferroli,²⁷ A. Calcaterra,²⁷ R. de Sangro,²⁷ G. Finocchiaro,²⁷ S. Pacetti,²⁷ P. Patteri,²⁷ I. M. Peruzzi,^{27,§} M. Piccolo,²⁷ M. Rama,²⁷ A. Zallo,²⁷ A. Buzzo,^{28a} R. Contri,^{28a,28b} M. Lo Vetere,^{28a,28b} M. M. Macri,^{28a} M. R. Monge,^{28a,28b} S. Passaggio,^{28a} C. Patrignani,^{28a,28b} E. Robutti,^{28a} A. Santroni,^{28a,28b} S. Tosi,^{28a,28b} K. S. Chaisanguanthum,²⁹ M. Morii,²⁹ J. Marks,³⁰ S. Schenk,³⁰ U. Uwer,³⁰ V. Klose,³¹ H. M. Lacker,³¹ D. J. Bard,³² P. D. Dauncey,³² J. A. Nash,³² W. Panduro Vazquez,³² M. Tibbetts,³² P. K. Behera,³³ X. Chai,³³ M. J. Charles,³³ U. Mallik,³³ J. Cochran,³⁴ H. B. Crawley,³⁴ L. Dong,³⁴ W. T. Meyer,³⁴ S. Prell,³⁴ E. I. Rosenberg,³⁴ A. E. Rubin,³⁴ Y. Y. Gao,³⁵ A. V. Gritsan,³⁵ Z. J. Guo,³⁵ C. K. Lae,³⁵ A. G. Denig,³⁶ M. Fritsch,³⁶ G. Schott,³⁶ N. Arnaud,³⁷ J. Béquilleux,³⁷ A. D'Orazio,³⁷ M. Davier,³⁷ J. Firmino da Costa,³⁷ G. Grosdidier,³⁷ A. Höcker,³⁷ V. Lepeltier,³⁷ F. Le Diberder,³⁷ A. M. Lutz,³⁷ S. Pruvot,³⁷ P. Roudeau,³⁷ M. H. Schune,³⁷ J. Serrano,³⁷ V. Sordini,^{37,||} A. Stocchi,³⁷ G. Wormser,³⁷ D. J. Lange,³⁸ D. M. Wright,³⁸ I. Bingham,³⁹ J. P. Burke,³⁹ C. A. Chavez,³⁹ J. R. Fry,³⁹ E. Gabathuler,³⁹ R. Gamet,³⁹ D. E. Hutchcroft,³⁹ D. J. Payne,³⁹ C. Touramanis,³⁹ A. J. Bevan,⁴⁰ C. K. Clarke,⁴⁰ K. A. George,⁴⁰ F. Di Lodovico,⁴⁰ R. Sacco,⁴⁰ M. Sigamani,⁴⁰ G. Cowan,⁴¹ H. U. Flaecher,⁴¹ D. A. Hopkins,⁴¹ S. Paramesvaran,⁴¹ F. Salvatore,⁴¹ A. C. Wren,⁴¹ D. N. Brown,⁴² C. L. Davis,⁴² K. E. Alwyn,⁴³ D. Bailey,⁴³ R. J. Barlow,⁴³ Y. M. Chia,⁴³ C. L. Edgar,⁴³ G. Jackson,⁴³ G. D. Lafferty,⁴³ T. J. West,⁴³ J. I. Yi,⁴³ J. Anderson,⁴⁴ C. Chen,⁴⁴ A. Jawahery,⁴⁴ D. A. Roberts,⁴⁴ G. Simi,⁴⁴ J. M. Tuggle,⁴⁴ C. Dallapiccola,⁴⁵ X. Li,⁴⁵ E. Salvati,⁴⁵ S. Saremi,⁴⁵ R. Cowan,⁴⁶ D. Dujmic,⁴⁶ P. H. Fisher,⁴⁶ K. Koeneke,⁴⁶ G. Sciolla,⁴⁶ M. Spitznagel,⁴⁶ F. Taylor,⁴⁶ R. K. Yamamoto,⁴⁶ M. Zhao,⁴⁶ P. M. Patel,⁴⁷ S. H. Robertson,⁴⁷ A. Lazzaro,^{48a,48b} V. Lombardo,^{48a} F. Palombo,^{48a,48b} J. M. Bauer,⁴⁹ L. Cremaldi,⁴⁹ V. Eschenburg,⁴⁹ R. Godang,^{49,¶} R. Kroeger,⁴⁹ D. A. Sanders,⁴⁹ D. J. Summers,⁴⁹ H. W. Zhao,⁴⁹ M. Simard,⁵⁰ P. Taras,⁵⁰ F. B. Viaud,⁵⁰ H. Nicholson,⁵¹ G. De Nardo,^{52a,52b} L. Lista,^{52a} D. Monorchio,^{52a,52b} G. Onorato,^{52a,52b} C. Sciacca,^{52a,52b} G. Raven,⁵³ H. L. Snoek,⁵³ C. P. Jessop,⁵⁴ K. J. Knoepfel,⁵⁴ J. M. LoSecco,⁵⁴ W. F. Wang,⁵⁴ G. Benelli,⁵⁵ L. A. Corwin,⁵⁵ K. Honscheid,⁵⁵ H. Kagan,⁵⁵ R. Kass,⁵⁵ J. P. Morris,⁵⁵ A. M. Rahimi,⁵⁵ J. J. Regensburger,⁵⁵ S. J. Sekula,⁵⁵ Q. K. Wong,⁵⁵ N. L. Blount,⁵⁶ J. Brau,⁵⁶ R. Frey,⁵⁶ O. Igonkina,⁵⁶ J. A. Kolb,⁵⁶ M. Lu,⁵⁶ R. Rahmat,⁵⁶ N. B. Sinev,⁵⁶ D. Strom,⁵⁶ J. Strube,⁵⁶ E. Torrence,⁵⁶ G. Castelli,^{57a,57b} N. Gagliardi,^{57a,57b} M. Margoni,^{57a,57b} M. Morandin,^{57a} M. Posocco,^{57a} M. Rotondo,^{57a} F. Simonetto,^{57a,57b} R. Stroili,^{57a,57b} C. Voci,^{57a,57b} P. del Amo Sanchez,⁵⁸ E. Ben-Haim,⁵⁸ H. Briand,⁵⁸ G. Calderini,⁵⁸ J. Chauveau,⁵⁸ P. David,⁵⁸ L. Del Buono,⁵⁸ O. Hamon,⁵⁸ Ph. Leruste,⁵⁸ J. Ocariz,⁵⁸ A. Perez,⁵⁸ J. Prendki,⁵⁸ S. Sitt,⁵⁸ L. Gladney,⁵⁹ M. Biasini,^{60a,60b} R. Covarelli,^{60a,60b} E. Manoni,^{60a,60b} C. Angelini,^{61a,61b} G. Batignani,^{61a,61b} S. Bettarini,^{61a,61b} M. Carpinelli,^{61a,61b,**} A. Cervelli,^{61a,61b} F. Forti,^{61a,61b} M. A. Giorgi,^{61a,61b} A. Lusiani,^{61a,61c} G. Marchiori,^{61a,61b} M. Morganti,^{61a,61b} N. Neri,^{61a,61b} E. Paoloni,^{61a,61b} G. Rizzo,^{61a,61b} J. J. Walsh,^{61a} D. Lopes Pegna,⁶² C. Lu,⁶² J. Olsen,⁶² A. J. S. Smith,⁶² A. V. Telnov,⁶² F. Anulli,^{63a} E. Baracchini,^{63a,63b} G. Cavoto,^{63a} D. del Re,^{63a,63b}

E. Di Marco,^{63a,63b} R. Faccini,^{63a,63b} F. Ferrarotto,^{63a} F. Ferroni,^{63a,63b} M. Gaspero,^{63a,63b} P.D. Jackson,^{63a} L. Li Gioi,^{63a} M. A. Mazzoni,^{63a} S. Morganti,^{63a} G. Piredda,^{63a} F. Polci,^{63a,63b} F. Renga,^{63a,63b} C. Voena,^{63a} M. Ebert,⁶⁴ T. Hartmann,⁶⁴ H. Schröder,⁶⁴ R. Waldi,⁶⁴ T. Adye,⁶⁵ B. Franek,⁶⁵ E. O. Olaiya,⁶⁵ F. F. Wilson,⁶⁵ S. Emery,⁶⁶ M. Escalier,⁶⁶ L. Esteve,⁶⁶ S. F. Ganzhur,⁶⁶ G. Hamel de Monchenault,⁶⁶ W. Kozanecki,⁶⁶ G. Vasseur,⁶⁶ Ch. Yèche,⁶⁶ M. Zito,⁶⁶ X. R. Chen,⁶⁷ H. Liu,⁶⁷ W. Park,⁶⁷ M. V. Purohit,⁶⁷ R. M. White,⁶⁷ J. R. Wilson,⁶⁷ M. T. Allen,⁶⁸ D. Aston,⁶⁸ R. Bartoldus,⁶⁸ P. Bechtel,⁶⁸ J. F. Benitez,⁶⁸ R. Cenci,⁶⁸ J. P. Coleman,⁶⁸ M. R. Convery,⁶⁸ J. C. Dingfelder,⁶⁸ J. Dorfan,⁶⁸ G. P. Dubois-Felsmann,⁶⁸ W. Dunwoodie,⁶⁸ R. C. Field,⁶⁸ A. M. Gabareen,⁶⁸ S. J. Gowdy,⁶⁸ M. T. Graham,⁶⁸ P. Grenier,⁶⁸ C. Hast,⁶⁸ W. R. Innes,⁶⁸ J. Kaminski,⁶⁸ M. H. Kelsey,⁶⁸ H. Kim,⁶⁸ P. Kim,⁶⁸ M. L. Kocian,⁶⁸ D. W. G. S. Leith,⁶⁸ S. Li,⁶⁸ B. Lindquist,⁶⁸ S. Luitz,⁶⁸ V. Luth,⁶⁸ H. L. Lynch,⁶⁸ D. B. MacFarlane,⁶⁸ H. Marsiske,⁶⁸ R. Messner,⁶⁸ D. R. Muller,⁶⁸ H. Neal,⁶⁸ S. Nelson,⁶⁸ C. P. O'Grady,⁶⁸ I. Ofte,⁶⁸ A. Perazzo,⁶⁸ M. Perl,⁶⁸ B. N. Ratcliff,⁶⁸ A. Roodman,⁶⁸ A. A. Salnikov,⁶⁸ R. H. Schindler,⁶⁸ J. Schwiening,⁶⁸ A. Snyder,⁶⁸ D. Su,⁶⁸ M. K. Sullivan,⁶⁸ K. Suzuki,⁶⁸ S. K. Swain,⁶⁸ J. M. Thompson,⁶⁸ J. Va'vra,⁶⁸ A. P. Wagner,⁶⁸ M. Weaver,⁶⁸ C. A. West,⁶⁸ W. J. Wisniewski,⁶⁸ M. Wittgen,⁶⁸ D. H. Wright,⁶⁸ H. W. Wulsin,⁶⁸ A. K. Yarritu,⁶⁸ K. Yi,⁶⁸ C. C. Young,⁶⁸ V. Ziegler,⁶⁸ P. R. Burchat,⁶⁹ A. J. Edwards,⁶⁹ S. A. Majewski,⁶⁹ T. S. Miyashita,⁶⁹ B. A. Petersen,⁶⁹ L. Wilden,⁶⁹ S. Ahmed,⁷⁰ M. S. Alam,⁷⁰ J. A. Ernst,⁷⁰ B. Pan,⁷⁰ M. A. Saeed,⁷⁰ S. B. Zain,⁷⁰ S. M. Spanier,⁷¹ B. J. Wogslund,⁷¹ R. Eckmann,⁷² J. L. Ritchie,⁷² A. M. Ruland,⁷² C. J. Schilling,⁷² R. F. Schwitters,⁷² B. W. Drummond,⁷³ J. M. Izen,⁷³ X. C. Lou,⁷³ F. Bianchi,^{74a,74b} D. Gamba,^{74a,74b} M. Pelliccioni,^{74a,74b} M. Bomben,^{75a,75b} L. Bosisio,^{75a,75b} C. Cartaro,^{75a,75b} G. Della Ricca,^{75a,75b} L. Lanceri,^{75a,75b} L. Vitale,^{75a,75b} V. Azzolini,⁷⁶ N. Lopez-March,⁷⁶ F. Martinez-Vidal,⁷⁶ D. A. Milanese,⁷⁶ A. Oyanguren,⁷⁶ J. Albert,⁷⁷ Sw. Banerjee,⁷⁷ B. Bhuyan,⁷⁷ H. H. F. Choi,⁷⁷ K. Hamano,⁷⁷ R. Kowalewski,⁷⁷ M. J. Lewczuk,⁷⁷ I. M. Nugent,⁷⁷ J. M. Roney,⁷⁷ R. J. Sobie,⁷⁷ T. J. Gershon,⁷⁸ P. F. Harrison,⁷⁸ J. Ilic,⁷⁸ T. E. Latham,⁷⁸ G. B. Mohanty,⁷⁸ H. R. Band,⁷⁹ X. Chen,⁷⁹ S. Dasu,⁷⁹ K. T. Flood,⁷⁹ Y. Pan,⁷⁹ M. Pierini,⁷⁹ R. Prepost,⁷⁹ C. O. Vuosalo,⁷⁹ and S. L. Wu⁷⁹

(BABAR Collaboration)

¹Laboratoire de Physique des Particules, IN2P3/CNRS et Université de Savoie, F-74941 Annecy-Le-Vieux, France

²Universitat de Barcelona, Facultat de Física, Departament ECM, E-08028 Barcelona, Spain

^{3a}INFN Sezione di Bari, I-70126 Bari, Italy

^{3b}Dipartimento di Fisica, Università di Bari, I-70126 Bari, Italy

⁴University of Bergen, Institute of Physics, N-5007 Bergen, Norway

⁵Lawrence Berkeley National Laboratory and University of California, Berkeley, California 94720, USA

⁶University of Birmingham, Birmingham, B15 2TT, United Kingdom

⁷Ruhr Universität Bochum, Institut für Experimentalphysik I, D-44780 Bochum, Germany

⁸University of Bristol, Bristol BS8 1TL, United Kingdom

⁹University of British Columbia, Vancouver, British Columbia, Canada V6T 1Z1

¹⁰Brunel University, Uxbridge, Middlesex UB8 3PH, United Kingdom

¹¹Budker Institute of Nuclear Physics, Novosibirsk 630090, Russia

¹²University of California at Irvine, Irvine, California 92697, USA

¹³University of California at Los Angeles, Los Angeles, California 90024, USA

¹⁴University of California at Riverside, Riverside, California 92521, USA

¹⁵University of California at San Diego, La Jolla, California 92093, USA

¹⁶University of California at Santa Barbara, Santa Barbara, California 93106, USA

¹⁷University of California at Santa Cruz, Institute for Particle Physics, Santa Cruz, California 95064, USA

¹⁸California Institute of Technology, Pasadena, California 91125, USA

¹⁹University of Cincinnati, Cincinnati, Ohio 45221, USA

²⁰University of Colorado, Boulder, Colorado 80309, USA

²¹Colorado State University, Fort Collins, Colorado 80523, USA

²²Technische Universität Dortmund, Fakultät Physik, D-44221 Dortmund, Germany

²³Technische Universität Dresden, Institut für Kern- und Teilchenphysik, D-01062 Dresden, Germany

²⁴Laboratoire Leprince-Ringuet, CNRS/IN2P3, Ecole Polytechnique, F-91128 Palaiseau, France

²⁵University of Edinburgh, Edinburgh EH9 3JZ, United Kingdom

^{26a}INFN Sezione di Ferrara, I-44100 Ferrara, Italy

^{26b}Dipartimento di Fisica, Università di Ferrara, I-44100 Ferrara, Italy

²⁷INFN Laboratori Nazionali di Frascati, I-00044 Frascati, Italy

^{28a}INFN Sezione di Genova, I-16146 Genova, Italy

^{28b}Dipartimento di Fisica, Università di Genova, I-16146 Genova, Italy

²⁹Harvard University, Cambridge, Massachusetts 02138, USA

- ³⁰*Universität Heidelberg, Physikalisches Institut, Philosophenweg 12, D-69120 Heidelberg, Germany*
- ³¹*Humboldt-Universität zu Berlin, Institut für Physik, Newtonstr. 15, D-12489 Berlin, Germany*
- ³²*Imperial College London, London, SW7 2AZ, United Kingdom*
- ³³*University of Iowa, Iowa City, Iowa 52242, USA*
- ³⁴*Iowa State University, Ames, Iowa 50011-3160, USA*
- ³⁵*Johns Hopkins University, Baltimore, Maryland 21218, USA*
- ³⁶*Universität Karlsruhe, Institut für Experimentelle Kernphysik, D-76021 Karlsruhe, Germany*
- ³⁷*Laboratoire de l'Accélérateur Linéaire, IN2P3/CNRS et Université Paris-Sud 11, Centre Scientifique d'Orsay, B. P. 34, F-91898 Orsay Cedex, France*
- ³⁸*Lawrence Livermore National Laboratory, Livermore, California 94550, USA*
- ³⁹*University of Liverpool, Liverpool L69 7ZE, United Kingdom*
- ⁴⁰*Queen Mary, University of London, London, E1 4NS, United Kingdom*
- ⁴¹*University of London, Royal Holloway and Bedford New College, Egham, Surrey TW20 0EX, United Kingdom*
- ⁴²*University of Louisville, Louisville, Kentucky 40292, USA*
- ⁴³*University of Manchester, Manchester M13 9PL, United Kingdom*
- ⁴⁴*University of Maryland, College Park, Maryland 20742, USA*
- ⁴⁵*University of Massachusetts, Amherst, Massachusetts 01003, USA*
- ⁴⁶*Massachusetts Institute of Technology, Laboratory for Nuclear Science, Cambridge, Massachusetts 02139, USA*
- ⁴⁷*McGill University, Montréal, Québec, Canada H3A 2T8*
- ^{48a}*INFN Sezione di Milano, I-20133 Milano, Italy*
- ^{48b}*Dipartimento di Fisica, Università di Milano, I-20133 Milano, Italy*
- ⁴⁹*University of Mississippi, University, Mississippi 38677, USA*
- ⁵⁰*Université de Montréal, Physique des Particules, Montréal, Québec, Canada H3C 3J7*
- ⁵¹*Mount Holyoke College, South Hadley, Massachusetts 01075, USA*
- ^{52a}*INFN Sezione di Napoli, I-80126 Napoli, Italy*
- ^{52b}*Dipartimento di Scienze Fisiche, Università di Napoli Federico II, I-80126 Napoli, Italy*
- ⁵³*NIKHEF, National Institute for Nuclear Physics and High Energy Physics, NL-1009 DB Amsterdam, The Netherlands*
- ⁵⁴*University of Notre Dame, Notre Dame, Indiana 46556, USA*
- ⁵⁵*Ohio State University, Columbus, Ohio 43210, USA*
- ⁵⁶*University of Oregon, Eugene, Oregon 97403, USA*
- ^{57a}*INFN Sezione di Padova, I-35131 Padova, Italy*
- ^{57b}*Dipartimento di Fisica, Università di Padova, I-35131 Padova, Italy*
- ⁵⁸*Laboratoire de Physique Nucléaire et de Hautes Energies, IN2P3/CNRS, Université Pierre et Marie Curie-Paris6, Université Denis Diderot-Paris7, F-75252 Paris, France*
- ⁵⁹*University of Pennsylvania, Philadelphia, Pennsylvania 19104, USA*
- ^{60a}*INFN Sezione di Perugia, I-06100 Perugia, Italy*
- ^{60b}*Dipartimento di Fisica, Università di Perugia, I-06100 Perugia, Italy*
- ^{61a}*INFN Sezione di Pisa, I-56127 Pisa, Italy*
- ^{61b}*Dipartimento di Fisica, I-56127 Pisa, Italy*
- ^{61c}*Università di Pisa, Scuola Normale Superiore di Pisa, I-56127 Pisa, Italy*
- ⁶²*Princeton University, Princeton, New Jersey 08544, USA*
- ^{63a}*INFN Sezione di Roma, I-00185 Roma, Italy*
- ^{63b}*Dipartimento di Fisica, Università di Roma La Sapienza, I-00185 Roma, Italy*
- ⁶⁴*Universität Rostock, D-18051 Rostock, Germany*
- ⁶⁵*Rutherford Appleton Laboratory, Chilton, Didcot, Oxon, OX11 0QX, United Kingdom*
- ⁶⁶*DSM/Irfu, CEA/Saclay, F-91191 Gif-sur-Yvette Cedex, France*
- ⁶⁷*University of South Carolina, Columbia, South Carolina 29208, USA*
- ⁶⁸*Stanford Linear Accelerator Center, Stanford, California 94309, USA*
- ⁶⁹*Stanford University, Stanford, California 94305-4060, USA*
- ⁷⁰*State University of New York, Albany, New York 12222, USA*
- ⁷¹*University of Tennessee, Knoxville, Tennessee 37996, USA*

*Deceased.

†Now at Temple University, Philadelphia, PA 19122, USA.

‡Now at Tel Aviv University, Tel Aviv, 69978, Israel.

§Also with Università di Perugia, Dipartimento di Fisica, Perugia, Italy.

||Also with Università di Roma La Sapienza, I-00185 Roma, Italy.

¶Now at University of South Alabama, Mobile, AL 36688, USA.

**Also with Università di Sassari, Sassari, Italy.

⁷²*University of Texas at Austin, Austin, Texas 78712, USA*⁷³*University of Texas at Dallas, Richardson, Texas 75083, USA*^{74a}*INFN Sezione di Torino, I-10125 Torino, Italy;*^{74b}*Dipartimento di Fisica Sperimentale, Università di Torino, I-10125 Torino, Italy*^{75a}*INFN Sezione di Trieste, I-34127 Trieste, Italy*^{75b}*Dipartimento di Fisica, Università di Trieste, I-34127 Trieste, Italy*⁷⁶*IFIC, Universitat de Valencia-CSIC, E-46071 Valencia, Spain*⁷⁷*University of Victoria, Victoria, British Columbia, Canada V8W 3P6*⁷⁸*Department of Physics, University of Warwick, Coventry CV4 7AL, United Kingdom*⁷⁹*University of Wisconsin, Madison, Wisconsin 53706, USA*

(Received 8 September 2008; published 15 January 2009)

Semileptonic \bar{B} decays to $DX\ell\bar{\nu}$ ($\ell = e$ or μ) are selected by reconstructing $D^0\ell$ and $D^+\ell$ combinations from a sample of 230×10^6 $Y(4S) \rightarrow B\bar{B}$ decays recorded with the BABAR detector at the PEP-II e^+e^- collider at SLAC. A global fit to these samples in a three-dimensional space of kinematic variables is used to determine the branching fractions $\mathcal{B}(B^- \rightarrow D^0\ell\bar{\nu}) = (2.34 \pm 0.03 \pm 0.13)\%$ and $\mathcal{B}(B^- \rightarrow D^{*0}\ell\bar{\nu}) = (5.40 \pm 0.02 \pm 0.21)\%$ where the errors are statistical and systematic, respectively. The fit also determines form-factor parameters in a parametrization based on heavy quark effective theory, resulting in $\rho_D^2 = 1.20 \pm 0.04 \pm 0.07$ for $\bar{B} \rightarrow D\ell\bar{\nu}$ and $\rho_{D^*}^2 = 1.22 \pm 0.02 \pm 0.07$ for $\bar{B} \rightarrow D^*\ell\bar{\nu}$. These values are used to obtain the product of the Cabibbo-Kobayashi-Maskawa matrix element $|V_{cb}|$ times the form factor at the zero recoil point for both $\bar{B} \rightarrow D\ell\bar{\nu}$ decays, $\mathcal{G}(1)|V_{cb}| = (43.1 \pm 0.8 \pm 2.3) \times 10^{-3}$, and for $\bar{B} \rightarrow D^*\ell\bar{\nu}$ decays, $\mathcal{F}(1)|V_{cb}| = (35.9 \pm 0.2 \pm 1.2) \times 10^{-3}$.

DOI: 10.1103/PhysRevD.79.012002

PACS numbers: 13.25.Hw, 12.15.Hh, 11.30.Er

I. INTRODUCTION

The study of semileptonic decays of heavy quarks provides the cleanest avenue for the determination of several elements of the Cabibbo-Kobayashi-Maskawa matrix [1], which are fundamental parameters in the standard model of particle physics. The coupling strength of the weak $b \rightarrow c$ transition is proportional to $|V_{cb}|$, which has been measured in both inclusive semileptonic B decays [2] and in the exclusive transitions $\bar{B} \rightarrow D\ell\bar{\nu}$ [3–6] and $\bar{B} \rightarrow D^*\ell\bar{\nu}$ [3,6–10] ($\ell = e$ or μ and charge conjugate modes are implied). The inclusive and exclusive determinations of $|V_{cb}|$ rely on different theoretical calculations. The former employs a parton-level calculation of the decay rate organized in a double expansion in α_S and in inverse powers of m_b , the b -quark mass. The latter relies on a parametrization of the decay form factors using heavy quark symmetry and a nonperturbative calculation of the form-factor normalization at the zero recoil (maximum squared momentum transfer) point. The theoretical uncertainties in these two approaches are independent. The inclusive and exclusive experimental measurements use different techniques and have negligible statistical overlap, and thus have largely uncorrelated uncertainties. This independence makes the comparison of $|V_{cb}|$ from inclusive and exclusive decays a powerful test of our understanding of semileptonic decays. The latest determinations [11] differ by more than 2 standard deviations (σ), and the inclusive determination is currently more than twice as precise as the exclusive determination. Improvements in the measurements of exclusive decays will strengthen this test. This is particularly

true for the $\bar{B} \rightarrow D\ell\bar{\nu}$ decay, where the experimental uncertainties dominate the determination of $|V_{cb}|$. For the decay $\bar{B}^0 \rightarrow D^{*+}\ell\bar{\nu}$, the experimental situation needs clarification, as existing measurements are in poor agreement with each other [11]. Finally, precise measurements of semileptonic B decays to charm are needed to further improve determinations of $|V_{ub}|$, where $\bar{B} \rightarrow D^{(*)}\ell\bar{\nu}$ decays are the principal background.

Semileptonic $b \rightarrow c$ transitions result in the production of a charm system that cascades down to the ground state D^0 or D^+ mesons. Most previous analyses have focused on reconstructing separately the exclusive decays $\bar{B} \rightarrow D^*\ell\bar{\nu}$ [3,7–10] and $\bar{B} \rightarrow D\ell\bar{\nu}$ [3–5]. The $\bar{B} \rightarrow D^*\ell\bar{\nu}$ analyses involve reconstruction of the soft transition pion from the decay $D^* \rightarrow D\pi$, which is at the limit of detector acceptance; determination of the reconstruction efficiency for these pions introduces significant systematic uncertainty. Studies of the exclusive decay $\bar{B} \rightarrow D\ell\bar{\nu}$ suffer from large feed-down background from $\bar{B} \rightarrow D^*\ell\bar{\nu}$ decays where the transition pion is undetected.

In this analysis we reconstruct $D^0\ell$ and $D^+\ell$ pairs and use a global fit to their kinematic properties to determine the branching fractions and form-factor parameters of the dominant semileptonic decays $\bar{B} \rightarrow D\ell\bar{\nu}$ and $\bar{B} \rightarrow D^*\ell\bar{\nu}$. The reconstructed $D\ell$ samples contain, by design, the feed-down from all the higher mass states (apart from decays of the type $\bar{B} \rightarrow D_s^+ X\ell\bar{\nu}$ [12]). Kinematic restrictions are imposed to reduce the contribution of backgrounds from semileptonic decays to final state hadronic systems more massive than D^* and from other sources of $D\ell$ combinations. Distributions from selected events are binned in the

three-dimensional space described below. The electron and muon samples are input into separate fits, in which isospin symmetry is assumed for the semileptonic decay rates. Semileptonic decays are produced via a spectator diagram in which the heavy quark decays independently; strong interaction corrections to this process conserve isospin. As a result, we constrain semileptonic decay rates for B^- and \bar{B}^0 to be equal, e.g., $\Gamma(B^- \rightarrow D^0 l^- \bar{\nu}) = \Gamma(\bar{B}^0 \rightarrow D^+ l^- \bar{\nu})$. This substantially reduces statistical uncertainties on the fitted parameters. Systematic uncertainties associated with the modeling of the signal and background processes, the detector response, and uncertainties on input parameters are determined, along with their correlations between the electron and muon samples. The fitted results are then combined using the full covariance matrix of statistical and systematic errors. For both $\bar{B} \rightarrow D \ell \bar{\nu}$ and $\bar{B} \rightarrow D^* \ell \bar{\nu}$ decays, the fitted branching fractions and form-factor parameters are used to determine the products $\mathcal{G}(1)|V_{cb}|$ and $\mathcal{F}(1)|V_{cb}|$. These measurements, along with theoretical input on the form-factor normalizations $\mathcal{G}(1)$ and $\mathcal{F}(1)$ at the zero recoil point, allow determinations of $|V_{cb}|$.

The approach taken in this study has some similarity to that of Ref. [6], where the branching fractions for $\bar{B} \rightarrow D \ell \bar{\nu}$ and $\bar{B} \rightarrow D^* \ell \bar{\nu}$ are measured simultaneously. However, Ref. [6] reconstructs semileptonic B decays in events in which the second B meson is fully reconstructed. That approach allows the use of the missing mass squared as a powerful discriminant. This analysis provides modest discrimination between the different semileptonic decays on an event-by-event basis, but results in a much larger statistical sample and enables the measurement of form-factor parameters.

The remaining sections of this paper are organized as follows. In Sec. II we describe the *BABAR* detector and the samples of *BABAR* data and simulated events used in the analysis. The event selection and the distributions that are input to the global fit are discussed in Sec. III. We give the parametrization of the form factors of $\bar{B} \rightarrow D^{(*)} \ell \bar{\nu}$ decays and the modeling of semileptonic \bar{B} decays to $D^{(*)} \pi$ and $D^{(*)} \pi \pi$ states in Sec. IV. The global fit strategy and results are given in Sec. V, and the evaluation of systematic uncertainties is detailed in Sec. VI. Section VII presents the determination of $|V_{cb}|$ from the fitted results. The final section, Sec. VIII, discusses the results and provides averages with previous *BABAR* measurements.

II. THE *BABAR* DETECTOR AND DATA SET

The data used in this analysis were collected with the *BABAR* detector at the PEP-II storage ring between 1999 and 2004. PEP-II is an asymmetric collider; the center of mass (CM) of the colliding e^+e^- moves with velocity $\beta = 0.49$ along the beam axis in the laboratory rest frame. The data collected at energies near the peak of the $Y(4S)$ resonance (on peak) correspond to 207 fb^{-1} or $230 \times$

$10^6 \bar{B}\bar{B}$ decays. Data collected just below the $\bar{B}\bar{B}$ threshold (off peak), corresponding to 21.5 fb^{-1} , are used to subtract the $e^+e^- \rightarrow q\bar{q}$ ($q = u, d, s, c$) background under the $Y(4S)$ resonance.

The *BABAR* detector is described in detail elsewhere [13]. It consists of a silicon vertex tracker (SVT), a drift chamber (DCH), a detector of internally reflected Cherenkov light (DIRC), an electromagnetic calorimeter (EMC), and an instrumented flux return (IFR). The SVT and DCH operate in an axial magnetic field of 1.5 T and provide measurements of the positions and momenta of charged particles, as well as of their ionization energy loss (dE/dx). Energy and shower shape measurements for photons and electrons are provided by the EMC. The DIRC measures the angle of Cherenkov photons emitted by charged particles traversing the fused silica radiator bars. Charged particles that traverse the EMC and showering hadrons are measured in the IFR as they penetrate successive layers of the return yoke of the magnet.

Simulated events used in the analysis are generated using the EVTGEN [14] program, and the generated particles are propagated through a model of the *BABAR* detector with the GEANT4 [15] program and reconstructed using the same algorithms used on *BABAR* data. The form-factor parametrization [16] used in the simulation for $\bar{B} \rightarrow D^* \ell \bar{\nu}$ decays is based on heavy quark effective theory (HQET) [17], while the ISGW2 model [18] is used for $\bar{B} \rightarrow D \ell \bar{\nu}$ and $\bar{B} \rightarrow D^{**} \ell \bar{\nu}$ decays, where D^{**} is one of the four P -wave charm mesons as described in Sec. III B. These are subsequently reweighted to the forms given in Sec. IV. For nonresonant $\bar{B} \rightarrow D^{(*)} \pi \ell \bar{\nu}$ decays, the Goity-Roberts model [19] is used. In order to saturate the inclusive semileptonic $b \rightarrow c \ell \bar{\nu}$ decay rate, we include a contribution from $\bar{B} \rightarrow D^{(*)} \pi \pi \ell \bar{\nu}$ decays; a variety of models are considered for this purpose. The branching fractions for B and charm decays in the simulation are rescaled to the values in Ref. [11]. In addition, the momentum spectra for D^0 and D^+ from $B \rightarrow DX$ and $\bar{B} \rightarrow DX$ decays are adjusted to agree with the corresponding measured spectra from Ref. [20]. This adjustment is done only for background processes.

The simulation of the detector response provided by the GEANT4-based program is further adjusted by comparing with *BABAR* data control samples. In particular, the efficiency of charged track reconstruction is modified by 1%–2%, depending on momenta and event multiplicity, based on studies of multihadron events and 1-versus-3 prong $e^+e^- \rightarrow \tau^+\tau^-$ events. The efficiencies and misidentification probabilities of the particle identification (PID) algorithms used to select pions, kaons, electrons, and muons (see Sec. III) are adjusted based on studies of samples of $e^+e^- \rightarrow e^+e^-\gamma$ and $e^+e^- \rightarrow \mu^+\mu^-\gamma$, and several samples reconstructed without particle identification: 1-versus-3 prong $e^+e^- \rightarrow \tau^+\tau^-$ events, $K_S^0 \rightarrow \pi^+\pi^-$, $D^{*+} \rightarrow D^0\pi^+ \rightarrow (K^-\pi^+)\pi^+$, and $\Lambda \rightarrow p\pi^-$.

III. EVENT SELECTION

A. Preselection of $D\ell$ candidates

We select multihadron events by requiring at least three good-quality charged tracks, a total reconstructed energy in the event exceeding 4.5 GeV, the second normalized Fox-Wolfram moment [21] $R_2 < 0.5$, and the distance between the interaction point and the primary vertex of the B decay to be less than 0.5 cm (6.0 cm) in the direction transverse (parallel) to the beam line. In these events an identified electron or muon candidate must be present, along with a candidate D meson decay. Candidate electrons are identified using a likelihood ratio based on the shower shape in the EMC, dE/dx in the tracking detectors, the Cherenkov angle, and the ratio of EMC energy to track momentum. The electron identification efficiency is 94% within the acceptance of the calorimeter, and the pion misidentification rate is 0.1%. Muon candidates are identified using a neural network that takes input information from the tracking detectors, EMC, and IFR. The muon identification efficiency rises with momentum to reach a plateau of 70% for laboratory momenta above 1.4 GeV/ c , and the pion misidentification rate is 3%.

Kaon candidates are required to satisfy particle identification criteria based on the dE/dx measured in the tracking detectors and the Cherenkov angle measured in the DIRC. Each kaon candidate is combined with one or two charged tracks of opposite sign to form a $D^0 \rightarrow K^- \pi^+$ or $D^+ \rightarrow K^- \pi^+ \pi^+$ candidate. Those combinations with invariant masses in the range $1.840 < m_{K\pi} < 1.888$ GeV/ c^2 are considered as D^0 candidates and those in the range $1.845 < m_{K\pi\pi} < 1.893$ GeV/ c^2 as D^+ candidates, respectively. Combinations in the ‘‘sideband’’ mass regions $1.816 < m_{K\pi} < 1.840$ GeV/ c^2 and $1.888 < m_{K\pi} < 1.912$ GeV/ c^2 ($1.821 < m_{K\pi\pi} < 1.845$ GeV/ c^2 and $1.893 < m_{K\pi\pi} < 1.917$ GeV/ c^2) are used to estimate the combinatorial background.

The charge of the kaon candidate is required to have the same sign as that of the candidate lepton. Each D -lepton combination in an event is fitted to both $\bar{B} \rightarrow D\ell$ and $D \rightarrow K^- \pi^+ (\pi^+)$ vertices using the algorithm described in Ref. [22]. The fit probabilities are required to exceed 0.01 for the $\bar{B} \rightarrow D^0\ell$ and $\bar{B} \rightarrow D^+\ell$ vertices and 0.001 for the D^0 and D^+ decay vertices. We require the absolute value of the cosine of the angle between the $D\ell$ momentum vector and the thrust axis of the remaining particles in the event to be smaller than 0.92 to further reduce background, most of which comes from $e^+e^- \rightarrow q\bar{q}$ ($q = u, d, s, c$) events.

The signal yields are determined by subtracting the estimated combinatorial background from the number of D candidates in the peak region. The combinatorial background is estimated using the number of candidates in the D mass sideband regions scaled by the ratio of the widths of the signal and sideband regions. This is equivalent to assuming a linear dependence of the combinatorial back-

ground on invariant mass. The change in the yields is negligible when using other assumptions for the background shape. Candidates from $e^+e^- \rightarrow q\bar{q}$ events are statistically removed from the data sample by subtracting the distribution of candidates observed in the data collected at energies below the $B\bar{B}$ threshold (off peak), after scaling these data by the factor $r_L = (\mathcal{L}_{\text{on}}^{S_{\text{off}}})/(\mathcal{L}_{\text{off}}^{S_{\text{on}}})$ to account for the difference in luminosity and the dependence of the annihilation cross section on energy. The selection criteria listed above were determined using simulated $B\bar{B}$ events and off-peak data to roughly maximize the statistical significance of the $D\ell$ signal yields in $e^+e^- \rightarrow B\bar{B}$ events. They have an overall efficiency of 80% (76%) for $\bar{B} \rightarrow D^0 X \ell \bar{\nu}$ ($\bar{B} \rightarrow D^+ X \ell \bar{\nu}$) decays with p_ℓ^* , the lepton momentum magnitude in the CM frame, in the range 0.8–2.8 GeV/ c .

The invariant mass distributions for the D^0 and D^+ candidates, after off-peak subtraction, are shown in Fig. 1 for two kinematic subsets representing regions with good and poor signal-to-background ratios. The small differences in peak position and combinatorial background level have a negligible impact on the analysis due to the sideband subtraction described above and the wide signal window.

The $D^0\ell$ and $D^+\ell$ candidates are binned in three kinematic variables:

- (i) p_D^* , the D momentum in the CM frame;
- (ii) p_ℓ^* , the lepton momentum in the CM frame;
- (iii) $\cos\theta_{B-D\ell} \equiv (2E_B^* E_{D\ell}^* - m_B^2 - m_{D\ell}^2)/(2p_B^* p_{D\ell}^*)$, the cosine of the angle between the \bar{B} and $D\ell$ momentum vectors in the CM frame under the assumption that the \bar{B} decayed to $D\ell\bar{\nu}$. If the $D\ell$ pair is not from a $\bar{B} \rightarrow D\ell\bar{\nu}$ decay, $|\cos\theta_{B-D\ell}|$ can exceed unity. The B energy and momentum are not measured event by event; they are calculated from the CM energy determined by the PEP-II beams as $E_B^* = \sqrt{s}/2$ and $p_B^* = \sqrt{E_B^{*2} - m_B^2}$, where m_B is the B^0 meson mass. The energy, momentum, and invariant mass corresponding to the sum of the D and lepton four-vectors in the CM frame are denoted $E_{D\ell}^*$, $p_{D\ell}^*$, and $m_{D\ell}$, respectively.

The binning in these three variables is discussed in Sec. III C.

B. Sources of $D\ell$ candidates

There are several sources of $D\ell$ candidates that survive the D -mass sideband and off-peak subtractions. In both the D^0 and D^+ samples we group them as follows (\bar{B} represents both B^- and \bar{B}^0):

- (i) $\bar{B} \rightarrow D\ell\bar{\nu}$,
- (ii) $\bar{B} \rightarrow D^* \ell \bar{\nu}$,
- (iii) $\bar{B} \rightarrow D^{(*)}(n\pi)\ell\bar{\nu}$, which includes the following:
 - (a) The P -wave D^{**} charm mesons. In the framework of HQET, the P -wave charm mesons are

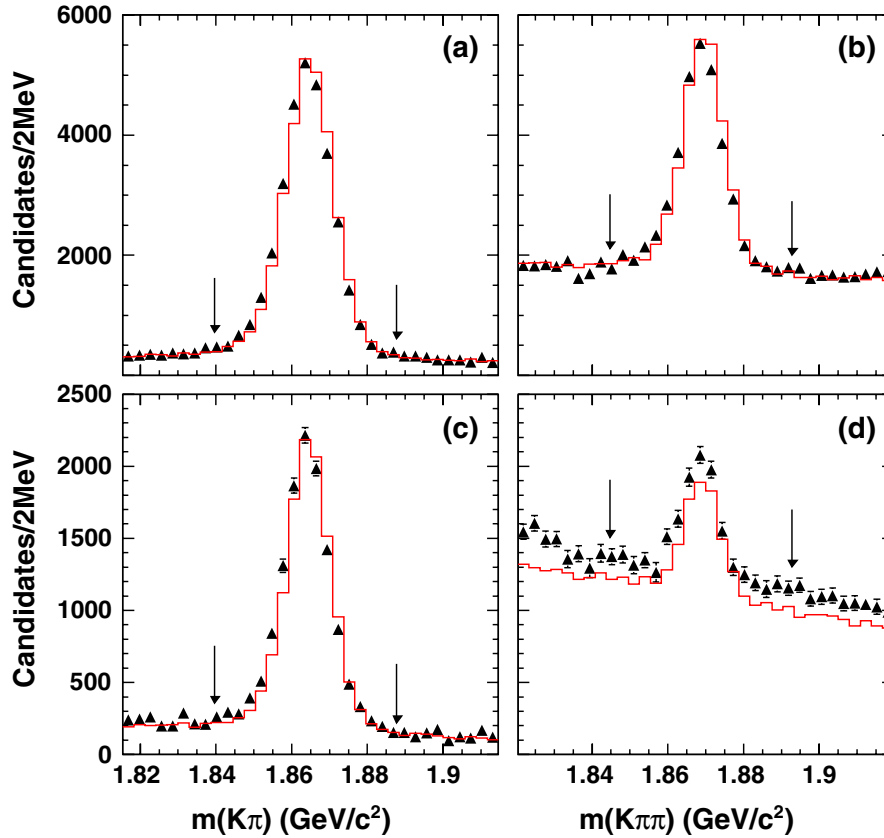


FIG. 1 (color online). The invariant mass distributions (data points) for selected candidates. Scaled off-peak data have been subtracted to remove contributions from $e^+e^- \rightarrow q\bar{q}$ annihilation. Plots (a, c) show $K^-\pi^+$ combinations and (b, d) show $K^-\pi^+\pi^+$ combinations. In each case the $D\ell$ candidates are required to satisfy $-2.0 < \cos\theta_{B-D\ell} < 1.1$. The further kinematic requirements are $1.6 < p_\ell^* < 1.8$ GeV/c, $1.6 < p_D^* < 2.0$ GeV/c for plots (a, b) and $2.0 < p_\ell^* < 2.35$ GeV/c, $0.8 < p_D^* < 1.2$ GeV/c for plots (c, d). The histograms show the contribution from simulated $B\bar{B}$ events scaled to the data luminosity. The arrows indicate the boundaries between signal and sideband regions.

categorized by the angular momentum of the light constituent, j_ℓ , namely, $j_\ell^P = 1/2^-$ doublet D_0^* and D_1^* and $j_\ell^P = 3/2^-$ doublet D_1 and D_2^* [23].

(b) Nonresonant $\bar{B} \rightarrow D^{(*)}\pi\ell\bar{\nu}$.

(c) Decays of the type $\bar{B} \rightarrow D^{(*)}\pi\pi\ell\bar{\nu}$; the modeling of these is discussed in Sec. IV D.

(iv) Background from $B\bar{B}$ events in which the lepton and D candidates do not arise from a single semileptonic \bar{B} decay. These include (in order of importance)

(a) Direct leptons from $\bar{B} \rightarrow X\ell\bar{\nu}$ decays combined with a D from the decay of the other B meson in the event. Roughly one-third of this background comes from events in which $B^0\bar{B}^0$ mixing results in the decay of two \bar{B}^0 mesons. Most of the remaining contribution comes from Cabibbo-Kobayashi-Maskawa-suppressed $B \rightarrow DX$ transitions.

(b) Uncorrelated cascade decays. In this case the lepton mostly comes from the decay of an anti-charm meson produced in the B decay and the

D arises from the decay of the other \bar{B} meson in the event.

(c) Correlated cascade decays, in which the lepton and D candidates come from the same parent \bar{B} meson. These are mainly $\bar{B} \rightarrow D\bar{D}(X)$ and $\bar{B} \rightarrow D(X)\tau\nu$ decays, with the lepton coming from the decay of an anticharm meson or tau.

(d) Misidentified lepton background. The probability of a hadron being misidentified as a lepton is negligible for electrons but not for muons.

As mentioned previously, the same decay widths are imposed for the semileptonic transitions of \bar{B}^0 and B^- . For the background processes (source iv) no such requirement is imposed.

C. Kinematic restrictions

Despite the use of the best available information for calculating the background and $\bar{B} \rightarrow D^{(*)}(n\pi)\ell\bar{\nu}$ distributions, these components suffer from significant uncertainties. We therefore restrict the kinematic range of the variables used in the fit to reduce the impact of these

TABLE I. Definitions of bins used for kinematic variables.

Quantity	Number of bins	Bin edges
$\cos\theta_{B-D\ell}$	3	-2.0, -1.0, 0.0, 1.1
p_ℓ^* (GeV/c)	10	1.2, 1.3, 1.4, 1.5, 1.6, 1.7, 1.8, 1.9, 2.0, 2.1, 2.35
p_D^* (GeV/c)	8	0.8, 1.1, 1.35, 1.5, 1.65, 1.8, 1.95, 2.1, 2.25

uncertainties while preserving sensitivity to the $\bar{B} \rightarrow D\ell\bar{\nu}$ and $\bar{B} \rightarrow D^*\ell\bar{\nu}$ branching fractions and form-factor parameters. We require $-2 < \cos\theta_{B-D\ell} < 1.1$ and place restrictions on p_D^* and p_ℓ^* , rejecting regions where the signal decays are not dominant. This results in the ranges $1.2 \text{ GeV}/c < p_\ell^* < 2.35 \text{ GeV}/c$ and $0.8 \text{ GeV}/c < p_D^* < 2.25 \text{ GeV}/c$. The yield within this region is 4.79×10^5 (2.95×10^5) candidates in the $D^0\ell$ ($D^+\ell$) sample with a statistical uncertainty of 0.26% (0.66%).

The data are binned finely enough to have good sensitivity to the fit parameters while maintaining adequate statistics per bin. Table I gives the binning used in the fit. We avoid setting a bin edge at $\cos\theta_{B-D\ell} = 1$ to reduce our sensitivity to the modeling of the resolution in this variable, since the $\bar{B} \rightarrow D\ell\bar{\nu}$ decay distribution has a sharp cutoff at this point.

Two-dimensional projections of the signal, background, and data distributions for the D^0e sample are shown in Fig. 2 to illustrate the separation power in these variables. The distributions for the $D^0\mu$ sample (not shown) are similar. The one-dimensional projections of the De and $D\mu$ samples are shown in Figs. 3 and 4. The difference in the size of the $\bar{B} \rightarrow D^*\ell\bar{\nu}$ components in $D^0\ell$ and $D^+\ell$ distributions is due to the fact that D^{*0} does not decay to D^+ .

IV. MODELING OF SEMILEPTONIC B DECAYS

In our fully simulated event samples $\bar{B} \rightarrow D\ell\bar{\nu}$ and $\bar{B} \rightarrow D^*\ell\bar{\nu}$ decays were generated using the ISGW2 model [18]. For $\bar{B} \rightarrow D^*\ell\bar{\nu}$ decays, a HQET model was used with a linear form-factor parametrization. We reweight

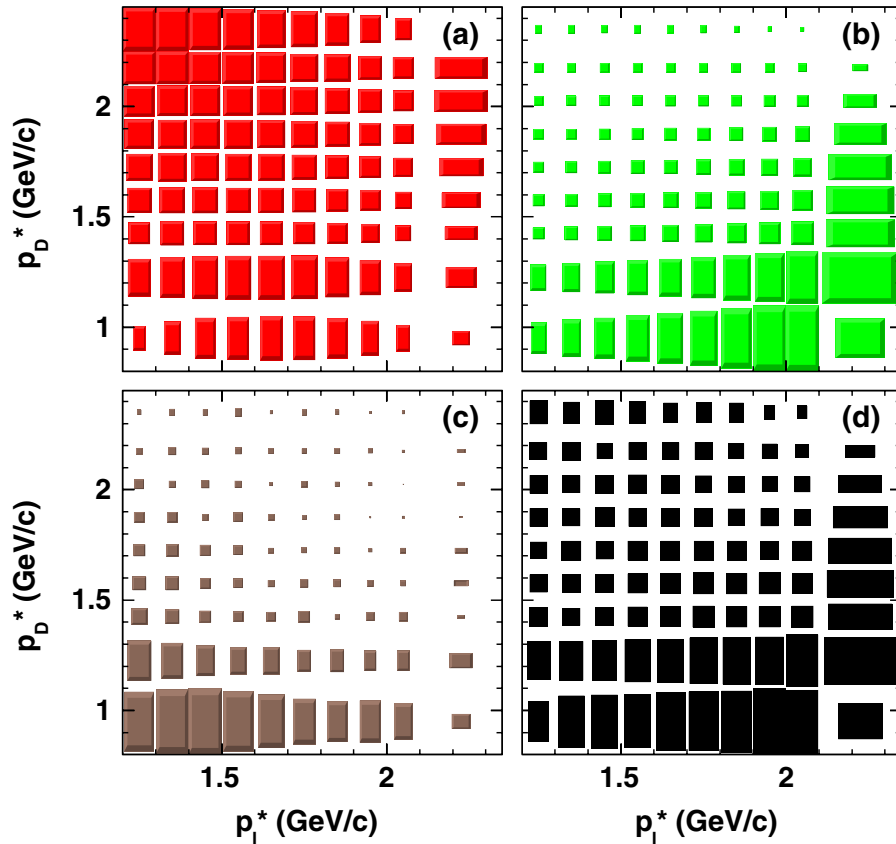


FIG. 2 (color online). Distribution of p_D^* vs p_ℓ^* for D^0e candidates after sideband subtraction. The shaded boxes have area proportional to the number of entries. The plots show simulated candidates for (a) $\bar{B} \rightarrow D e \bar{\nu}$, (b) $\bar{B} \rightarrow D^* e \bar{\nu}$, and (c) other (sources iii and iv combined), and for data after off-peak subtraction (d). The binning given in Table I is used, and only candidates that satisfy $0.0 < \cos\theta_{B-D\ell} < 1.1$ are plotted.

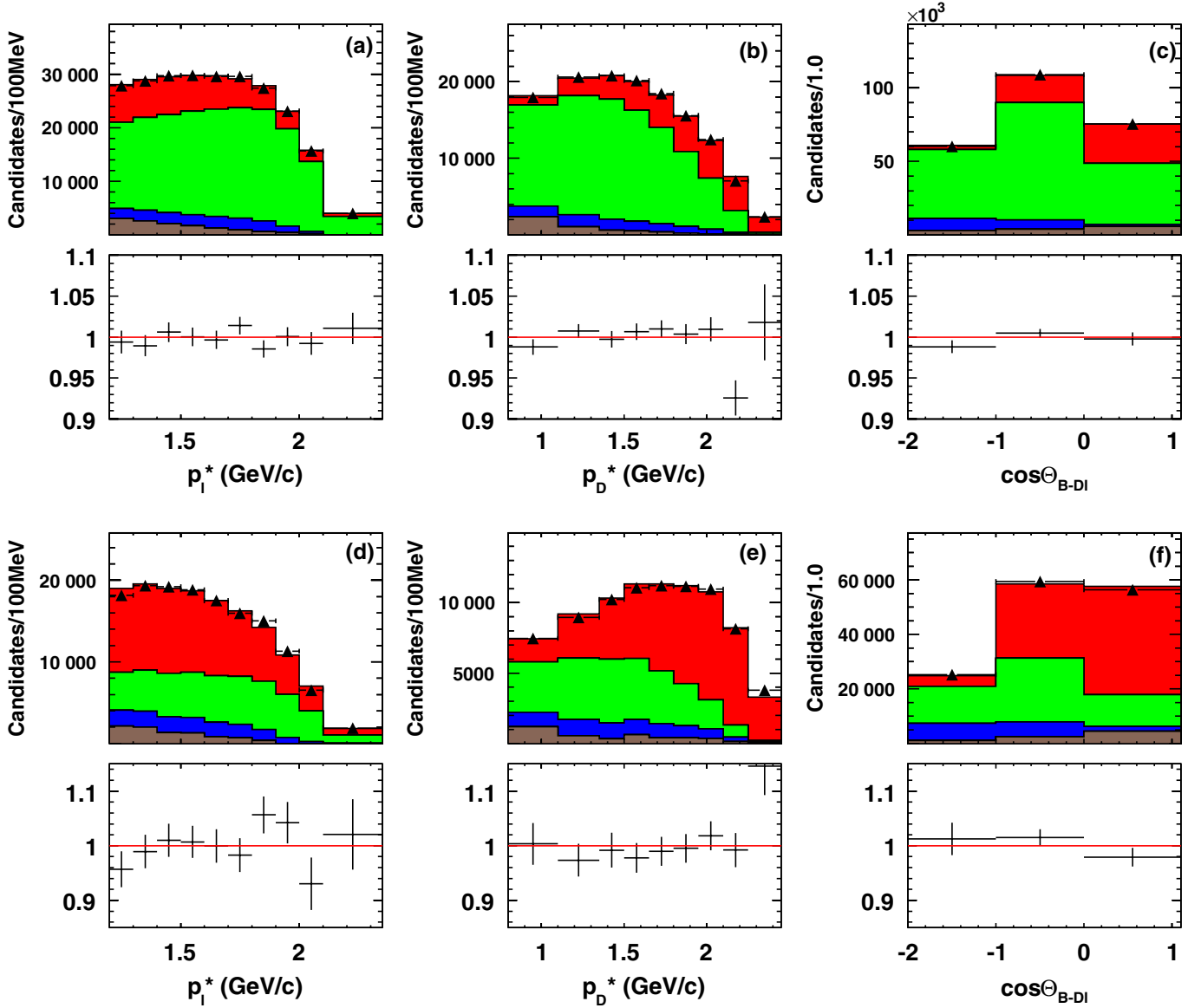


FIG. 3 (color online). Projections onto individual kinematic variables of the data after off-peak subtraction and the results of the fit: (a, d) lepton and (b, e) D momentum in the CM frame, and (c, f) $\cos\theta_{B-D\ell}$. The points show data for accepted $D^0 e$ (a, b, c) and $D^+ e$ (d, e, f) candidates, and the histograms show the individual fit components (from top to bottom): $\bar{B} \rightarrow D e \bar{\nu}$, $\bar{B} \rightarrow D^* e \bar{\nu}$, $\bar{B} \rightarrow D^{(*)}(n\pi) e \bar{\nu}$, and other $B\bar{B}$ background. The ratio of data to the sum of the fitted yields is shown below each plot.

all these decays using the formulas given in the following subsections. The histograms in Figs. 3 and 4 are reweighted.

A. $\bar{B} \rightarrow D \ell \bar{\nu}$ decays

The differential decay rate is given by [17]

$$\frac{d\Gamma(\bar{B} \rightarrow D \ell \bar{\nu})}{dw} = \frac{G_F^2 |V_{cb}|^2 m_B^5}{48\pi^3} r^3 (w^2 - 1)^{3/2} \times [(1+r)h_+(w) - (1-r)h_-(w)]^2, \quad (1)$$

where G_F is the Fermi constant, $h_+(w)$ and $h_-(w)$ are the form factors, $r \equiv m_D/m_B$ is the mass ratio, and m_B and m_D

are the B and D meson masses, respectively. The velocity transfer w is defined as

$$w \equiv v_B \cdot v_D, \quad (2)$$

where v_B and v_D are the four-velocities of the B and D mesons, respectively. In the B rest frame w corresponds to the Lorentz boost of the D meson. In the HQET model, the form factors are given by [16]

$$h_+(w) = \mathcal{G}(1) \times [1 - 8\rho_D^2 z + (51\rho_D^2 - 10)z^2 - (252\rho_D^2 - 84)z^3] \quad (3)$$

and

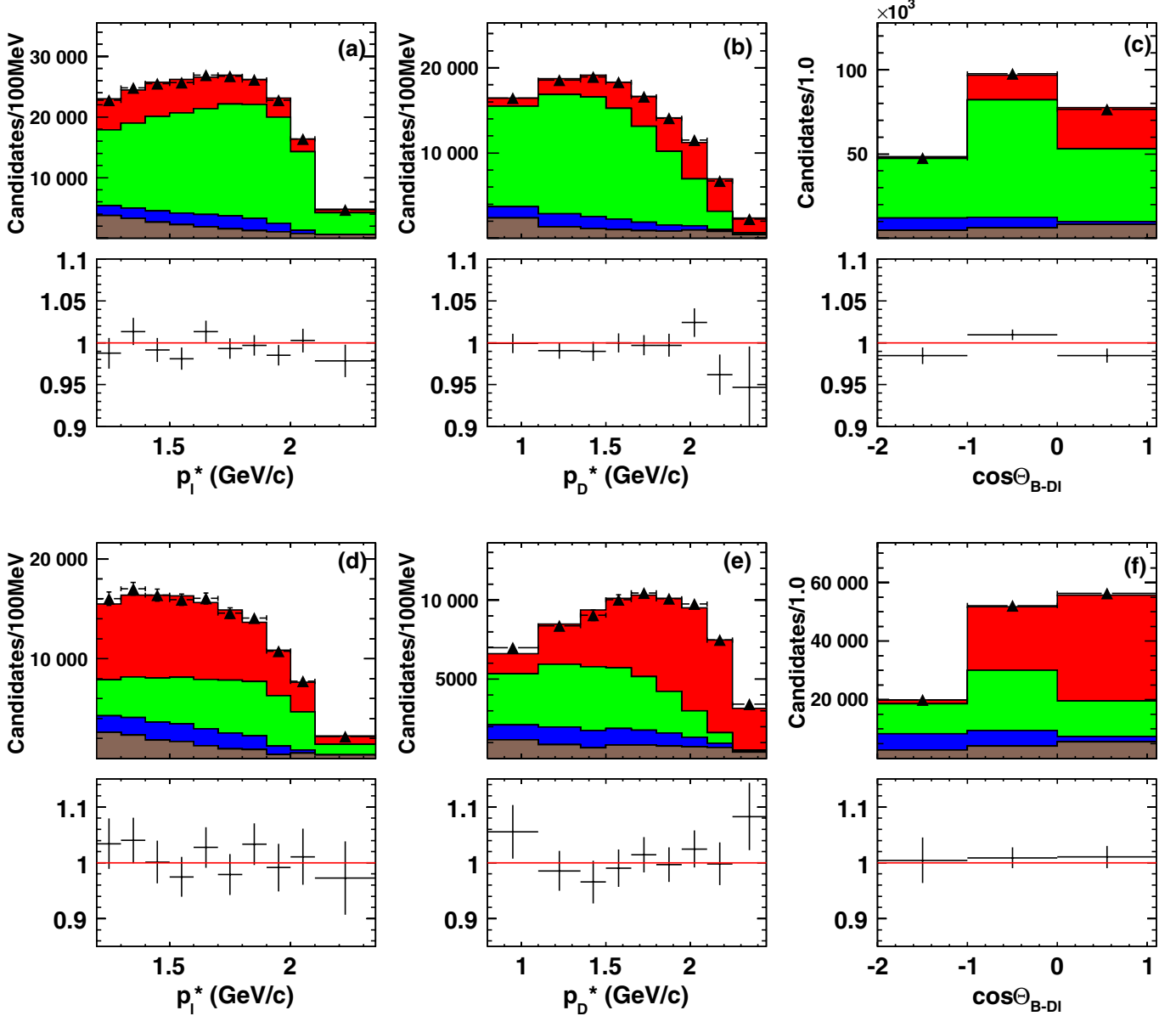


FIG. 4 (color online). Projections onto individual kinematic variables of the data after off-peak subtraction and the results of the fit: (a, d) lepton and (b, e) D momentum in the CM frame, and (c, f) $\cos\theta_{B-D\ell}$. The points show data for accepted $D^0\mu$ (a, b, c) and $D^+\mu$ (d, e, f) candidates, and the histograms show the individual fit components (from top to bottom): $\bar{B} \rightarrow D\mu\bar{\nu}$, $\bar{B} \rightarrow D^*\mu\bar{\nu}$, $\bar{B} \rightarrow D^{(*)}(n\pi)\mu\bar{\nu}$, and other $B\bar{B}$ background. The ratio of data to the sum of the fitted yields is shown below each plot.

$$h_-(w) = 0, \quad (4) \quad \text{following factor:}$$

where $z = (\sqrt{w+1} - \sqrt{2})/(\sqrt{w+1} + \sqrt{2})$ and ρ_D^2 and $\mathcal{G}(1)$ are, respectively, the form-factor slope and normalization at $w = 1$.

The above formulas neglect the lepton mass m_ℓ . Muon mass effects need to be included to achieve precision at the few percent level on the form-factor parameters. Allowing for nonzero lepton mass introduces additional terms in the phase space and form-factor expressions [24] that can be included by multiplying the decay rate formula by the

$$W_D = \left(1 - \frac{1}{1 + r^2 - 2rw} \frac{m_\ell^2}{m_B^2}\right)^2 \left[1 + \mathcal{K}_D(w) \frac{m_\ell^2}{m_B^2}\right] \quad (5)$$

where

$$\mathcal{K}_D(w) \equiv \left[1 + 3\left(\frac{1-r}{1+r}\right)^2 \left(\frac{w+1}{w-1}\right)\right] \frac{1}{2(1+r^2-2rw)}. \quad (6)$$

B. $\bar{B} \rightarrow D^* \ell \bar{\nu}$ decays

We need three additional kinematic variables to describe this decay. A common choice is θ_ℓ , θ_V , and χ , shown in Fig. 5, and defined as

- (i) θ_ℓ : the angle between the lepton and the direction opposite the B meson in the W rest frame.

- (ii) θ_V : the angle between the D meson and the direction opposite the B meson in the D^* rest frame.
 (iii) χ : the azimuthal angle between the planes formed by the W - ℓ and $D^* - D$ systems in the B rest frame.

The differential decay rate is given by [17]

$$\begin{aligned} \frac{d\Gamma(\bar{B} \rightarrow D^* \ell \bar{\nu})}{dwd \cos \theta_V d \cos \theta_\ell d\chi} = & \frac{3G_F^2}{4(4\pi)^4} |V_{cb}|^2 m_B m_{D^*}^2 \sqrt{w^2 - 1} (1 + r^{*2} - 2r^*w) [(1 - \cos \theta_\ell)^2 \sin^2 \theta_V |H_+(w)|^2 \\ & + (1 + \cos \theta_\ell)^2 \sin^2 \theta_V |H_-(w)|^2 + 4 \sin^2 \theta_\ell \cos^2 \theta_V |H_0(w)|^2 \\ & - 4 \sin \theta_\ell (1 - \cos \theta_\ell) \sin \theta_V \cos \theta_V \cos \chi H_+(w) H_0(w) \\ & + 4 \sin \theta_\ell (1 + \cos \theta_\ell) \sin \theta_V \cos \theta_V \cos \chi H_-(w) H_0(w) - 2 \sin^2 \theta_\ell \sin^2 \theta_V \cos 2\chi H_+(w) H_-(w)], \end{aligned} \quad (7)$$

where $H_i(w)$ are form factors, $r^* = m_{D^*}/m_B$, and m_{D^*} is the D^* meson mass. The $H_i(w)$ are usually written in terms of one form factor $h_{A_1}(w)$ and two form-factor ratios, $R_1(w)$ and $R_2(w)$, as follows:

$$H_i = -m_B \frac{R^*(1 - r^{*2})(w + 1)}{2\sqrt{1 + r^{*2} - 2r^*w}} h_{A_1}(w) \tilde{H}_i(w), \quad (8)$$

where $R^* = (2\sqrt{m_B m_{D^*}})/(m_B + m_{D^*})$ and

$$\tilde{H}_\pm(w) = \frac{\sqrt{1 + r^{*2} - 2r^*w}}{1 - r^*} \left(1 \mp \sqrt{\frac{w-1}{w+1}} R_1(w) \right), \quad (9)$$

$$\tilde{H}_0(w) = 1 + \frac{w-1}{1-r^*} (1 - R_2(w)).$$

The form-factor ratios have a modest dependence on w , estimated [16] as

$$\begin{aligned} R_1(w) &= R_1 - 0.12(w-1) + 0.05(w-1)^2, \\ R_2(w) &= R_2 + 0.11(w-1) - 0.06(w-1)^2. \end{aligned} \quad (10)$$

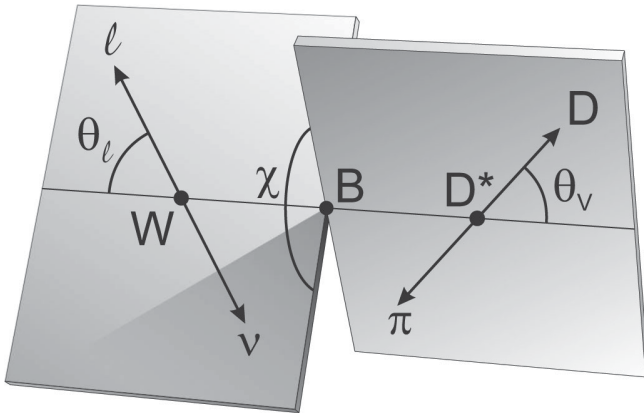


FIG. 5. Definition of the three angles θ_ℓ , θ_V , and χ for the decay $\bar{B} \rightarrow D^* \ell \bar{\nu}$.

The form used for $h_{A_1}(w)$ is [16]

$$\begin{aligned} h_{A_1}(w) &= \mathcal{F}(1) [1 - 8\rho_{D^*}^2 z + (53\rho_{D^*}^2 - 15)z^2 \\ &\quad - (231\rho_{D^*}^2 - 91)z^3], \end{aligned} \quad (11)$$

where $\rho_{D^*}^2$ and $\mathcal{F}(1)$ are, respectively, the form-factor slope and normalization at $w = 1$.

Nonzero lepton mass is accounted for by multiplying the decay rate formula by the factor

$$W_{D^*} = \left(1 - \frac{1}{1 + r^{*2} - 2r^*w} \frac{m_\ell^2}{m_B^2} \right)^2 \left[1 + \mathcal{K}_{D^*}(w) \frac{m_\ell^2}{m_B^2} \right], \quad (12)$$

where

$$\mathcal{K}_{D^*}(w) \equiv \left[1 + \frac{3}{2} \frac{\tilde{H}_t^2}{\tilde{H}_+^2 + \tilde{H}_-^2 + \tilde{H}_0^2} \right] \frac{1}{2(1 + r^{*2} - 2r^*w)}. \quad (13)$$

Here, \tilde{H}_t is expressed, using another form-factor ratio $R_3(w)$, by

$$\tilde{H}_t(w) = \frac{\sqrt{w^2 - 1}}{1 - r^*} \left(1 + \frac{r^* - w}{w + 1} R_3 - \frac{1 + r^{*2} - 2r^*w}{r^*(w + 1)} R_2 \right). \quad (14)$$

We take $R_3(w) = 1$; this approximation has a negligible impact on our fit results.

C. $\bar{B} \rightarrow D^{(*)} \pi \ell \bar{\nu}$ decays

The four P -wave D^{**} states have been measured in semileptonic decays [25–28]. The decays $\bar{B} \rightarrow D^{**} \ell \bar{\nu}$ are modeled following a HQET-inspired form-factor parametrization given in Ref. [23]. Detailed formulas are given in the Appendix. We use the approximation B₁ of this model for our main fit and use the approximation B₂ to evaluate the uncertainty due to the approximation. The slope of the

TABLE II. Input parameters for the fit.

Parameter	Value
R_1	$1.429 \pm 0.061 \pm 0.044$
R_2	$0.827 \pm 0.038 \pm 0.022$
D^{**} FF slope	-1.5 ± 0.5
$\mathcal{B}(B^- \rightarrow D^{(*)} \pi \ell \bar{\nu})$	0.0151 ± 0.0015
$f_{D_2^*/D_1}$	0.74 ± 0.20
$f_{D_0^* D \pi / D_1 D_2^*}$	0.87 ± 0.43
$f_{D_1^* D^* \pi / D_1 D_2^*}$	0.36 ± 0.30
$f_{D \pi / D_0^*}$	0.21 ± 0.21
$f_{D^* \pi / D_1^*}$	0.14 ± 0.14
$\mathcal{B}(B^- \rightarrow D^{(*)} \pi \pi \ell \bar{\nu})$	0.011 ± 0.011
$f_{D_2^*}$	1.7 ± 0.4
$\mathcal{B}(D^{*+} \rightarrow D^0 \pi^+)$	0.677 ± 0.005
$\mathcal{B}(D^0 \rightarrow K^- \pi^+)$	0.0389 ± 0.0005
$\mathcal{B}(D^+ \rightarrow K^- \pi^+ \pi^+)$	0.0922 ± 0.0021
τ_{B^-} / τ_{B^0}	1.071 ± 0.009
f_{+-} / f_{00}	1.065 ± 0.026

form factors versus w is parametrized by $\hat{\tau}'$, which we set to -1.5 and vary between -1.0 and -2.0 to study systematic uncertainties (Table II).

To parametrize the $\bar{B} \rightarrow D^{(*)} \pi \ell \bar{\nu}$ decay branching fractions we define five branching fraction ratios:

$$f_{D_2^*/D_1} \equiv \frac{\mathcal{B}(B^- \rightarrow D_2^{*0} \ell \bar{\nu})}{\mathcal{B}(B^- \rightarrow D_1^0 \ell \bar{\nu})}, \quad (15)$$

$$f_{D \pi / D_0^*} \equiv \frac{\mathcal{B}^{\text{NR}}(B^- \rightarrow D^+ \pi^- \ell \bar{\nu})}{\mathcal{B}(B^- \rightarrow D_0^{*0} \ell \bar{\nu})}, \quad (16)$$

$$f_{D^* \pi / D_1^*} \equiv \frac{\mathcal{B}^{\text{NR}}(B^- \rightarrow D^{*+} \pi^- \ell \bar{\nu})}{\mathcal{B}(B^- \rightarrow D_1^{*0} \ell \bar{\nu})}, \quad (17)$$

$$f_{D_0^* D \pi / D_1 D_2^*} \equiv \frac{\mathcal{B}(B^- \rightarrow D_0^{*0} \ell \bar{\nu}) + \mathcal{B}^{\text{NR}}(B^- \rightarrow D \pi \ell \bar{\nu})}{\mathcal{B}(B^- \rightarrow D_1^0 \ell \bar{\nu}) + \mathcal{B}(B^- \rightarrow D_2^{*0} \ell \bar{\nu})}, \quad (18)$$

$$f_{D_1^* D^* \pi / D_1 D_2^*} \equiv \frac{\mathcal{B}(B^- \rightarrow D_1^{*0} \ell \bar{\nu}) + \mathcal{B}^{\text{NR}}(B^- \rightarrow D^* \pi \ell \bar{\nu})}{\mathcal{B}(B^- \rightarrow D_1^0 \ell \bar{\nu}) + \mathcal{B}(B^- \rightarrow D_2^{*0} \ell \bar{\nu})}, \quad (19)$$

where NR stands for ‘‘nonresonant’’ decays, which are assumed to be isospin invariant. The quantity $f_{D_2^*/D_1}$ is the ratio between two narrow states, $f_{D \pi / D_0^*}$ ($f_{D^* \pi / D_1^*}$) is between two broad states decaying to $D \pi$ ($D^* \pi$), and the other two ratios are between broad and narrow states. With these definitions the branching fractions for individual modes can be related to the total branching fraction $\mathcal{B}(B^- \rightarrow D^{(*)} \pi \ell \bar{\nu}) \equiv \mathcal{B}(B^- \rightarrow D \pi \ell \bar{\nu}) + \mathcal{B}(B^- \rightarrow D^* \pi \ell \bar{\nu})$. We combine a new measurement [6] with the world average [11] to determine the value given in Table II.

TABLE III. Assumed masses, widths, and spins of the four hypothetical high-mass states contributing to $\bar{B} \rightarrow D^{(*)} \pi \pi \ell \bar{\nu}$ decays.

Name	Mass (GeV/ c^2)	Width (GeV)	Spin
X_c	2.61	0.3	0
X_c^*	2.61	0.3	1
Y_c	2.87	0.1	0
Y_c^*	2.87	0.1	1

To estimate the branching fraction ratios, we average several measurements [25–28] to find

$$\begin{aligned} \mathcal{B}(B^- \rightarrow D_1^0 \ell \bar{\nu}) &= 0.0042 \pm 0.0004, \\ \mathcal{B}(B^- \rightarrow D_2^{*0} \ell \bar{\nu}) &= 0.0031 \pm 0.0005, \\ \mathcal{B}(B^- \rightarrow D_1^{*0} \ell \bar{\nu}) &= 0.0022 \pm 0.0014, \\ \mathcal{B}(B^- \rightarrow D_0^{*0} \ell \bar{\nu}) &= 0.0048 \pm 0.0008. \end{aligned} \quad (20)$$

The sum of the D^{**} branching fractions saturates $\mathcal{B}(B^- \rightarrow D^{(*)} \pi \ell \bar{\nu})$ which implies that the nonresonant branching fractions are small. We use

$$\begin{aligned} \mathcal{B}^{\text{NR}}(B^- \rightarrow D \pi \ell \bar{\nu}) &= 0.0015 \pm 0.0015, \\ \mathcal{B}^{\text{NR}}(B^- \rightarrow D^* \pi \ell \bar{\nu}) &= 0.00045 \pm 0.00045. \end{aligned} \quad (21)$$

From these numbers the branching fraction ratios are calculated and listed in Table II. These quantities are taken as independent when evaluating systematic uncertainties.

D. $\bar{B} \rightarrow D^{(*)} \pi \pi \ell \bar{\nu}$ decays

Recent measurements [6,11] indicate that the inclusive $\bar{B} \rightarrow X_c \ell \bar{\nu}$ branching fraction is not saturated by the sum of the $\bar{B} \rightarrow D \ell \bar{\nu}$, $\bar{B} \rightarrow D^* \ell \bar{\nu}$, and $\bar{B} \rightarrow D^{(*)} \pi \ell \bar{\nu}$ branching fractions. In order to fill the gap, we include $\bar{B} \rightarrow D^{(*)} \pi \pi \ell \bar{\nu}$ decays in our fit. We assume the branching fraction of these decays, given in Table II, is equal to this missing contribution to the inclusive branching fraction [11].

The $\bar{B} \rightarrow D^{(*)} \pi \pi \ell \bar{\nu}$ decays are modeled as a combination of four resonances: pseudoscalar (X_c) and vector (X_c^*) states just above the $D^* \pi \pi$ threshold, and a heavier pair of pseudoscalar (Y_c) and vector (Y_c^*) states just above the $D^* \rho$ threshold, as listed in Table III. Each state is assumed to be produced with an equal rate in semileptonic B decays and each is assumed to decay with an equal branching fraction to $D \pi \pi$ and $D^* \pi \pi$, conserving isospin. These assumptions are varied in assessing systematic uncertainties.

V. GLOBAL FIT

The binned distributions of $D^0 \ell$ and $D^+ \ell$ candidates in the variables p_ℓ^* , p_D^* , and $\cos \theta_{B-D\ell}$ are fitted with the sum of distributions for the signal and background sources listed in Sec. III B. The expected shape of the individual

components is based on simulation, and the fit adjusts the normalization of each component to minimize the global chi-squared:

$$\chi^2(\vec{\alpha}) = \sum_{\text{bin } i} \frac{(N_i^{\text{on}} - r_{\mathcal{L}} N_i^{\text{off}} - \sum_j r_j C_j M_{ij})^2}{(\sigma_i^{\text{on}})^2 + r_{\mathcal{L}}^2 (\sigma_i^{\text{off}})^2 + \sum_j r_j^2 C_j^2 (\sigma_{ij}^{\text{MC}})^2}, \quad (22)$$

where the index i sums over bins of the $D^0 \ell$ and $D^+ \ell$ distributions and j sums over individual simulated components. The coefficients C_j depend on $\vec{\alpha}$, the set of free parameters determined by minimizing χ^2 . For example, for the $B^- \rightarrow D^0 \ell \bar{\nu}$ component the coefficient C_j is given by the ratio of the fitted $\mathcal{B}(B^- \rightarrow D^0 \ell \bar{\nu})$ branching fraction to the value used in generating the corresponding distribution. The number of candidates in the data collected on (below) the $Y(4S)$ peak in bin i is denoted N_i^{on} (N_i^{off}) and M_{ij} is the number of simulated events in bin i from source j . The M_{ij} may depend on $\vec{\alpha}$ as explained below. The statistical uncertainties, after D mass sideband subtraction, are given by the σ_i for the data and the σ_{ij} for the different Monte Carlo samples. The factor r_j is the ratio of the on-peak luminosity to the effective luminosity of the appropriate Monte Carlo sample. Only those bins in which the number of entries expected from the simulation exceeds 10 are used in the χ^2 sum.

For the $\bar{B} \rightarrow D \ell \bar{\nu}$ and $\bar{B} \rightarrow D^* \ell \bar{\nu}$ signal components we fit for both the branching fractions and for form-factor parameters. To facilitate this, we split these components into subcomponents, one corresponding to each unique combination of the parameters $\vec{\alpha}$ in the expression for the decay rate. In terms of the notation used in Eq. (22), we set

$$C_j M_{ij} = \sum_k C_j^{(k)} M_{ij}^{(k)}, \quad (23)$$

where the index k runs over the subcomponents. For example, the form factor in $\bar{B} \rightarrow D \ell \bar{\nu}$ decays is of the form $\mathcal{G}(z, \rho_D^2) = A(z) - \rho_D^2 B(z)$, where ρ_D^2 , the slope of the form factor, is a parameter in the fit and z is a kinematic variable. The decay rate, which depends on the square of \mathcal{G} , has terms proportional to 1, ρ_D^2 and $(\rho_D^2)^2$, thus requiring three subcomponents with coefficients $C_j^{(1)}$ to $C_j^{(3)}$. The calculation of the variance for the $\bar{B} \rightarrow D \ell \bar{\nu}$ component involves the fourth power of \mathcal{G} and thus requires five

subcomponents. For the $\bar{B} \rightarrow D^* \ell \bar{\nu}$ decay we use 18 subcomponents to allow the fitting of the form-factor parameters R_1, R_2 , and $\rho_{D^*}^2$ and 75 subcomponents to calculate the associated variance. By breaking the components up in this way the fitted parameters enter only as multiplicative factors on specific component histograms, $M_{ij}^{(k)}$, which allows us to use premade histograms to recalculate expected yields, avoids the need to loop over the simulated events at each step in the χ^2 minimization process, and results in a dramatic reduction in the required computation time.

A. Fit parameters and inputs

The semileptonic decay widths of $\bar{B} \rightarrow D \ell \bar{\nu}$, $\bar{B} \rightarrow D^* \ell \bar{\nu}$, and $\bar{B} \rightarrow D^{**} \ell \bar{\nu}$ are required to be equal for B^+ and B^0 . We also require isospin invariance in the decays $D^{**} \rightarrow D^{(*)} \pi$. As a result, the C_j depend on the following quantities: $\mathcal{B}(B^- \rightarrow D^0 \ell \bar{\nu})$ and the form-factor slope ρ_D^2 for $\bar{B} \rightarrow D \ell \bar{\nu}$ and $\mathcal{B}(B^- \rightarrow D^* \ell \bar{\nu})$, and form-factor parameters R_1, R_2 , and $\rho_{D^*}^2$ for $\bar{B} \rightarrow D^* \ell \bar{\nu}$. We fix R_1 and R_2 to the values obtained in Ref. [9]. The background contributions are kept at the values determined in the simulation. The overall normalizations of the $\bar{B} \rightarrow D^{(*)} \pi \ell \bar{\nu}$ and $\bar{B} \rightarrow D^{(*)} \pi \pi \ell \bar{\nu}$ components are also fixed. For the relevant D decay branching fractions we use the values from Ref. [11]. The values of the input parameters are listed in Table II, where $f_{D_2^*}$ is defined as the ratio $\mathcal{B}(D_2^{*+} \rightarrow D^0 \pi^+) / \mathcal{B}(D_2^{*+} \rightarrow D^{*0} \pi^+)$ [11,26], and f_{+-} / f_{00} is the ratio of branching fractions $\mathcal{B}(Y(4S) \rightarrow B^+ B^-) / \mathcal{B}(Y(4S) \rightarrow B^0 \bar{B}^0)$ [11]. All fixed values are varied in assessing systematic uncertainties.

B. Fit results

The fit is performed separately on the electron and muon samples. The results of these fits are given in Table IV. Both fits give good χ^2 probabilities. The corresponding \bar{B}^0 branching fractions are obtained from the B^- results by dividing by the lifetime ratio [11] $\tau_{B^-} / \tau_{\bar{B}^0} = 1.071$. The statistical correlations for the electron and muon samples are given in Table V. Figures 3 and 4 show the projected distributions on the three kinematic variables for the electron and muon samples along with the ratio of data over the fit.

TABLE IV. Fit results on the electron and muon samples, and their combination. The first error is statistical, the second systematic. (n.d.f. stands for number of degrees of freedom.)

Parameters	De sample	$D\mu$ sample	Combined result
ρ_D^2	$1.23 \pm 0.05 \pm 0.08$	$1.13 \pm 0.07 \pm 0.09$	$1.20 \pm 0.04 \pm 0.07$
$\rho_{D^*}^2$	$1.23 \pm 0.02 \pm 0.07$	$1.24 \pm 0.03 \pm 0.07$	$1.22 \pm 0.02 \pm 0.07$
$\mathcal{B}(D^0 \ell \bar{\nu})(\%)$	$2.38 \pm 0.03 \pm 0.14$	$2.26 \pm 0.04 \pm 0.16$	$2.34 \pm 0.03 \pm 0.13$
$\mathcal{B}(D^{*0} \ell \bar{\nu})(\%)$	$5.45 \pm 0.03 \pm 0.22$	$5.27 \pm 0.04 \pm 0.37$	$5.40 \pm 0.02 \pm 0.21$
$\chi^2/\text{n.d.f. (probability)}$	422/470 (0.94)	494/467 (0.19)	2.2/4 (0.71)

TABLE V. Statistical correlation coefficients between parameters from the fits to the electron and muon samples.

	<i>De</i> sample			<i>Dμ</i> sample		
	ρ_D^2	$\rho_{D^*}^2$	$\mathcal{B}(D)$	ρ_D^2	$\rho_{D^*}^2$	$\mathcal{B}(D)$
$\rho_{D^*}^2$	-0.299			-0.302		
$\mathcal{B}(D)$	+0.307	+0.180		+0.279	+0.198	
$\mathcal{B}(D^*)$	-0.388	+0.075	-0.526	-0.396	+0.069	-0.519

TABLE VI. Correlation coefficients for systematic errors. The upper and lower diagonal blocks correspond to electrons and muons, respectively.

	<i>De</i> sample				<i>Dμ</i> sample		
	ρ_D^2	$\rho_{D^*}^2$	$\mathcal{B}(D)$	$\mathcal{B}(D^*)$	ρ_D^2	$\rho_{D^*}^2$	$\mathcal{B}(D)$
$\rho_{D^*}^2$	-0.02						
$\mathcal{B}(D)$	+0.74	+0.08					
$\mathcal{B}(D^*)$	-0.22	+0.36	+0.31				
ρ_D^2	+0.75	-0.17	+0.47	-0.35			
$\rho_{D^*}^2$	-0.07	+0.98	+0.02	+0.31	-0.15		
$\mathcal{B}(D)$	+0.46	+0.00	+0.64	+0.17	+0.16	-0.03	
$\mathcal{B}(D^*)$	-0.17	+0.19	+0.12	+0.54	-0.48	+0.17	+0.67

The results of the separate fits to the *De* and *Dμ* samples are combined using the full 8×8 covariance matrix. This matrix is built from a block-diagonal statistical covariance matrix, with one 4×4 block coming from the fit to each lepton sample, and the full 8×8 systematic covariance matrix described in Sec. VI. The systematic covariance matrix consists of 4×4 matrices for the electron and muon parameters and a 4×4 set of electron-muon covariance terms. The corresponding correlation coefficients are given in Table VI. There is an advantage to combining the electron and muon results after the systematic errors have been evaluated; the results are weighted optimally (e.g., the difference in lepton identification efficiency uncertainties is taken into account) and the χ^2 from the combination provides a valid measure of the compatibility of the electron and muon results. The combined results are given in Table IV, and the correlation coefficients corresponding to the combined statistical and systematic errors are given in Table VII.

C. Fit validation

The fit was validated in several ways. A large number of simulated experiments were generated based on random

TABLE VII. Output correlation matrix for combined samples.

	ρ_D^2	$\rho_{D^*}^2$	$\mathcal{B}(D)$
$\rho_{D^*}^2$	-0.129		
$\mathcal{B}(D)$	+0.609	+0.023	
$\mathcal{B}(D^*)$	-0.285	+0.308	+0.283

samples drawn from the histograms used in the fit. The fit was performed on these simulated experiments to check for biases in the fitted values or associated variances. Small biases in the fitted values of several parameters—in no case exceeding 0.1 standard deviations for both electron and muon samples—were found. Given the smallness of the biases we do not correct the fit results. Additional sets of simulated experiments were generated with alternative values for the parameters. In each case the fit reproduced the alternative values within statistical uncertainties. An independent sample of fully simulated events was also used to validate the fit.

Additional fits were performed on the data to look for inconsistencies and quantify the impact of additional constraints. The electron and muon samples were combined before fitting; the results were compatible with expectations. Data samples collected in different years were fitted separately; the fit results agree within statistical uncertainties. The minimum number of expected entries per bin was varied from 10 to 100; the impact on the fitted parameters was negligible. Different binnings in the variables p_ℓ^* , $p_{D^*}^*$, and $\cos\theta_{B-D\ell}$ were tried; the fit results were in each case consistent with the nominal values. The boundaries of the *D* mass peak and sideband regions were varied by ± 2 MeV/ c^2 ; the impact on the fitted parameters was negligible.

Additional fits were performed in which R_1 and R_2 were treated as free parameters. The results, including associated systematic uncertainties, are given in Table VIII. Correlation coefficients for the combined fit are given in Table IX. The three D^* form-factor parameters are highly

TABLE VIII. Results on the electron, muon, and combined samples when fitting R_1 and R_2 .

Parameters	De sample	$D\mu$ sample	Combined result
ρ_D^2	$1.22 \pm 0.05 \pm 0.10$	$1.10 \pm 0.07 \pm 0.10$	$1.16 \pm 0.04 \pm 0.08$
$\rho_{D^*}^2$	$1.34 \pm 0.05 \pm 0.09$	$1.33 \pm 0.06 \pm 0.09$	$1.33 \pm 0.04 \pm 0.09$
R_1	$1.59 \pm 0.09 \pm 0.15$	$1.53 \pm 0.10 \pm 0.17$	$1.56 \pm 0.07 \pm 0.15$
R_2	$0.67 \pm 0.07 \pm 0.10$	$0.68 \pm 0.08 \pm 0.10$	$0.66 \pm 0.05 \pm 0.09$
$\mathcal{B}(D^0 \ell \bar{\nu})(\%)$	$2.38 \pm 0.04 \pm 0.15$	$2.25 \pm 0.04 \pm 0.17$	$2.32 \pm 0.03 \pm 0.13$
$\mathcal{B}(D^{*0} \ell \bar{\nu})(\%)$	$5.50 \pm 0.05 \pm 0.23$	$5.34 \pm 0.06 \pm 0.37$	$5.48 \pm 0.04 \pm 0.22$
$\chi^2/\text{n.d.f. (probability)}$	416/468 (0.96)	488/464 (0.21)	2.0/6 (0.92)

TABLE IX. Output correlation coefficients for combined samples with R_1 and R_2 fitted.

	ρ_D^2	$\rho_{D^*}^2$	R_1	R_2	$\mathcal{B}(D)$
$\rho_{D^*}^2$	-0.435				
R_1	-0.252	+0.752			
R_2	+0.519	-0.787	-0.740		
$\mathcal{B}(D)$	+0.602	-0.056	+0.114	+0.102	
$\mathcal{B}(D^*)$	-0.310	+0.406	+0.139	-0.309	+0.212

correlated. Comparing this set of parameters with the previous measurement [9], we find they are consistent at the 36% C.L.

VI. SYSTEMATIC STUDIES

There are several sources of systematic uncertainty in this analysis. Table X summarizes the systematic uncertainties on the quantities of interest; these were used in determining the systematic errors and correlations given in Tables IV and VI.

The parameters R_1 and R_2 are varied taking their correlation (-0.84) into account. We transform R_1 and R_2 into a set of parameters R'_1 and R'_2 that diagonalize the error matrix, and vary R'_1 and R'_2 independently. The D^{**} form-factor shape is varied in two ways: the slope is varied from -2.0 to -1.0 , and the approximation B_1 from Ref. [23] is replaced with B_2 (see also the Appendix). The total and relative branching fractions of the D^{**} components in $\bar{B} \rightarrow D^{(*)} \pi \ell \bar{\nu}$ decays are varied independently using the values in Table II. The D^*/D ratio of nonresonant decays, which is defined by $\mathcal{B}^{\text{NR}}(\bar{B} \rightarrow D^* \pi \ell \bar{\nu})/\mathcal{B}^{\text{NR}}(\bar{B} \rightarrow D \pi \ell \bar{\nu})$, is 0.3 in the nominal fit; we vary the ratio from 0.1 to 1.0. The branching fraction of $\bar{B} \rightarrow D^{(*)} \pi \pi \ell \bar{\nu}$ decays is varied as given in Table II, and the production ratios for the states used to model $\bar{B} \rightarrow D^{(*)} \pi \pi \ell \bar{\nu}$ decays, X_c^*/X_c , Y_c^*/Y_c , X_c/Y_c , and X_c^*/Y_c^* , are varied independently from 0.5 to 2.0. To evaluate the effect of $D_1 \rightarrow D \pi \pi$ decays [29], one-half of the $\bar{B} \rightarrow D^{(*)} \pi \pi \ell \bar{\nu}$ component is replaced by $D_1 \rightarrow D \pi \pi$ decays; the differences in fitted values are taken as systematic uncertainties.

The other parameters listed in Table II are also varied within their uncertainties. The determination of the number

of $B\bar{B}$ events introduces a normalization uncertainty of 1.1% on the branching fractions. The uncertainty in the luminosity ratio between on-peak and off-peak data is 0.25%.

The B momentum distribution is determined from the well-measured beam energy and B^0 mass. The uncertainty of 0.2 MeV in the beam energy measurement leads to a systematic error. Uncertainties arising from the simulation of the detector response to charged particle reconstruction and particle identification are studied by varying the efficiencies and misidentification probabilities based on comparisons between data and simulation on dedicated control samples. The uncertainty arising from radiative corrections is studied by comparing the results using PHOTOS [30] to simulate final state radiation (default case) with those obtained with PHOTOS turned off. We take 25% of the difference as an error. The uncertainty in the simulation of bremsstrahlung is based on an understanding of the detector material from studies of photon conversions and hadronic interactions. The uncertainty associated with the charge particle vertex requirements for the D and B decay points is evaluated by loosening the vertex probability cuts. The uncertainty arising from $B^0\bar{B}^0$ mixing is negligible.

Branching fractions in background simulations are varied within their measured uncertainties [11]. The inclusive differential branching fractions versus D momentum for B meson decays to D^0 , \bar{D}^0 , D^+ , and D^- mesons, which affect some background components, are varied using the measurements from Ref. [20].

The overall covariance matrix for the eight fitted quantities (four electron and four muon parameters) is built from the individual systematic variations as follows. For each variation taken, an eight-component vector $\Delta\vec{\alpha}$ of

TABLE X. Systematic uncertainties on fitted parameters, given in %. Numbers are negative when the fitted value decreases as the input parameter increases.

Item	Electron sample						Muon sample					
	ρ_D^2	$\rho_{D^*}^2$	$\mathcal{B}(D\ell\bar{\nu})$	$\mathcal{B}(D^*\ell\bar{\nu})$	$\mathcal{G}(1) V_{cb} $	$\mathcal{F}(1) V_{cb} $	ρ_D^2	$\rho_{D^*}^2$	$\mathcal{B}(D\ell\bar{\nu})$	$\mathcal{B}(D^*\ell\bar{\nu})$	$\mathcal{G}(1) V_{cb} $	$\mathcal{F}(1) V_{cb} $
R_1'	0.44	2.74	0.71	-0.38	0.60	0.71	0.50	2.67	0.74	-0.40	0.63	0.70
R_2'	-0.40	1.02	-0.18	0.30	-0.32	0.49	-0.45	0.96	-0.19	0.30	-0.33	0.48
D^{**} slope	-1.42	-2.52	-0.07	-0.09	-0.82	-0.87	-1.42	-2.58	-0.10	-0.10	-0.77	-0.92
D^{**} FF approximation	-0.87	0.33	-0.12	0.19	-0.54	0.20	-0.99	0.59	-0.12	0.21	-0.59	0.30
$\mathcal{B}(B^- \rightarrow D^{(*)}\pi\ell\bar{\nu})$	0.28	-0.27	-0.22	-0.80	0.04	-0.49	0.59	-0.32	-0.13	-0.86	0.24	-0.54
$f_{D_2^*/D_1}$	-0.39	0.16	-0.38	0.16	-0.41	0.13	-0.50	0.17	-0.41	0.18	-0.47	0.15
$f_{D_0^*D\pi/D_1D_2^*}$	-2.30	1.12	-1.53	0.97	-2.07	0.85	-3.13	1.23	-1.53	1.02	-2.41	0.93
$f_{D_1^*D^*\pi/D_1D_2^*}$	1.82	-1.14	1.30	-0.65	1.65	-0.70	2.44	-1.15	1.35	-0.72	1.91	-0.75
$f_{D\pi/D_0^*}$	-0.88	-1.28	0.36	0.17	-0.31	-0.34	-0.83	-1.23	0.31	0.18	-0.27	-0.33
$f_{D^*\pi/D_1^*}$	-0.21	-0.05	-0.13	0.21	-0.18	0.09	-0.30	-0.04	-0.15	0.23	-0.23	0.10
NR D^*/D ratio	0.58	-0.16	0.11	-0.09	0.38	-0.04	0.66	-0.16	0.11	-0.09	0.40	-0.03
$\mathcal{B}(B^- \rightarrow D^{(*)}\pi\pi\ell\bar{\nu})$	1.19	-1.97	0.25	-1.28	0.78	-1.28	1.98	-1.71	0.40	-1.20	1.20	-1.18
X^*/X and Y^*/Y ratio	0.61	-1.15	0.09	-0.27	0.39	-0.52	0.74	-1.02	0.08	-0.24	0.42	-0.47
X/Y and X^*/Y^* ratio	0.76	-0.83	0.21	-0.65	0.52	-0.60	1.09	-0.76	0.25	-0.63	0.68	-0.57
$D_1 \rightarrow D\pi\pi$	2.22	-1.54	0.74	-1.08	1.63	-1.05	2.74	-1.48	0.76	-1.06	1.81	-1.03
$f_{D_2^*}$	-0.14	-0.01	-0.10	0.07	-0.12	0.03	-0.16	-0.01	-0.10	0.07	-0.13	0.03
$\mathcal{B}(D^{*+} \rightarrow D^0\pi^+)$	0.73	-0.01	0.43	-0.34	0.62	-0.17	0.80	-0.00	0.41	-0.33	0.61	-0.17
$\mathcal{B}(D^0 \rightarrow K^-\pi^+)$	0.69	0.02	-0.21	-1.63	0.29	-0.80	0.92	0.12	-0.27	-1.68	0.35	-0.80
$\mathcal{B}(D^+ \rightarrow K^-\pi^+\pi^+)$	-1.46	-0.42	-2.17	0.30	-1.89	0.01	-1.43	-0.42	-2.10	0.28	-1.77	-0.01
τ_{B^-}/τ_{B^0}	0.26	0.16	0.63	0.27	0.46	0.19	0.22	0.16	0.58	0.28	0.41	0.19
f_{+-}/f_{00}	0.88	0.43	0.66	-0.53	0.82	-0.12	0.91	0.48	0.57	-0.52	0.75	-0.10
Number of $B\bar{B}$ events	0.00	-0.00	-1.11	-1.11	-0.55	-0.55	0.00	-0.00	-1.11	-1.11	-0.55	-0.55
Off-peak luminosity	0.05	0.01	-0.02	-0.00	0.02	0.00	0.07	0.00	-0.02	-0.00	0.02	-0.00
B momentum distribution	-0.96	0.63	1.29	-0.54	-1.15	0.48	1.30	-0.10	1.27	-0.64	1.31	-0.35
Lepton PID efficiency	0.52	0.16	1.21	0.82	0.90	0.46	3.30	0.06	5.11	5.83	1.99	2.90
Lepton mis-ID	0.03	0.01	-0.01	-0.01	0.01	-0.00	2.65	0.70	-0.59	-0.50	1.06	-0.01
Kaon PID	0.07	0.80	0.28	0.23	0.18	0.38	1.02	0.71	0.35	0.29	0.70	0.39
Tracking efficiency	-1.02	-0.43	-3.35	-2.00	-2.25	-1.15	-0.63	-0.28	-3.37	-2.09	-2.02	-1.14
Radiative corrections	-3.13	-1.04	-2.87	-0.74	-3.02	-0.71	-0.76	-0.61	-0.82	-0.25	-0.79	-0.33
Bremsstrahlung	0.07	0.00	-0.13	-0.28	-0.04	-0.14	0.00	0.00	0.00	0.00	0.00	0.00
Vertexing	0.83	-0.64	0.63	0.60	0.78	0.09	1.79	-0.76	0.97	0.54	1.41	0.01
Background total	1.39	1.12	0.64	0.34	1.07	0.51	1.58	1.09	0.67	0.38	1.16	0.49
Total	6.25	5.66	6.01	4.03	5.99	3.20	8.12	5.47	7.35	7.07	6.06	4.23

parameter differences between the alternative fit and the nominal fit is recorded. The ij element of the systematic error covariance matrix is the sum over all systematic variations k :

$$V_{\text{sys},ij} = \sum_k \Delta\alpha_i^{(k)} \Delta\alpha_j^{(k)}. \quad (24)$$

The corresponding correlation matrix is given in Table VI.

VII. DETERMINATION OF $|V_{cb}|$

The combined fit results with their full covariance matrix are used to calculate $\mathcal{G}(1)|V_{cb}|$ and $\mathcal{F}(1)|V_{cb}|$:

$$\mathcal{G}(1)|V_{cb}| = (43.1 \pm 0.8 \pm 2.3) \times 10^{-3}, \quad (25)$$

$$\mathcal{F}(1)|V_{cb}| = (35.9 \pm 0.2 \pm 1.2) \times 10^{-3}. \quad (26)$$

The errors are statistical and systematic, respectively. The associated correlations are +0.64 [between $\mathcal{G}(1)|V_{cb}|$ and

ρ_D^2], +0.56 [$\mathcal{F}(1)|V_{cb}|$ and $\rho_{D^*}^2$], and -0.07 [$\mathcal{G}(1)|V_{cb}|$ and $\mathcal{F}(1)|V_{cb}|$].

Using the values of $\mathcal{F}(1)|V_{cb}|$ and $\mathcal{G}(1)|V_{cb}|$ given above along with calculations of the form-factor normalizations allows one to determine $|V_{cb}|$. Using a recent lattice QCD calculation, $\mathcal{G}(1) = 1.074 \pm 0.018 \pm 0.016$ [31], multiplied by the electroweak correction [32] of 1.007, we find

$$D\ell\nu: |V_{cb}| = (39.9 \pm 0.8 \pm 2.2 \pm 0.9) \times 10^{-3}, \quad (27)$$

where the errors are statistical, systematic, and theoretical, respectively. For $\bar{B} \rightarrow D^*\ell\bar{\nu}$ we use a lattice QCD calculation of the form factor, $\mathcal{F}(1) = 0.921 \pm 0.013 \pm 0.020$ [33], along with the electroweak correction factor, to find

$$D^*\ell\nu: |V_{cb}| = (38.6 \pm 0.2 \pm 1.3 \pm 1.0) \times 10^{-3}. \quad (28)$$

The fits with R_1 and R_2 as free parameters give

$$\mathcal{G}(1)|V_{cb}| = (42.8 \pm 0.9 \pm 2.3) \times 10^{-3}, \quad (29)$$

$$\mathcal{F}(1)|V_{cb}| = (35.6 \pm 0.3 \pm 1.0) \times 10^{-3}, \quad (30)$$

with correlation coefficients +0.92 [between $\mathcal{G}(1)|V_{cb}|$ and ρ_D^2], +0.41 [$\mathcal{F}(1)|V_{cb}|$ and $\rho_{D^*}^2$], and -0.03 [$\mathcal{G}(1)|V_{cb}|$ and $\mathcal{F}(1)|V_{cb}|$].

VIII. DISCUSSION

The branching fractions and slope parameters measured here for $\bar{B} \rightarrow D\ell\bar{\nu}$ and $\bar{B} \rightarrow D^*\ell\bar{\nu}$ are consistent with the world averages [25] for these quantities. The measurements of ρ_D^2 and $\mathcal{G}(1)|V_{cb}|$ represent significant improvements on existing knowledge. The experimental technique used here, namely, a simultaneous global fit to $\bar{B} \rightarrow D^0X\ell\bar{\nu}$ and $\bar{B} \rightarrow D^+X\ell\bar{\nu}$ combinations, is complementary to previous measurements. In particular, it does not rely on the reconstruction of the soft transition pion from the $D^* \rightarrow D\pi$ decay.

The results obtained here, which are given in Table IV, can be combined with the existing *BABAR* measurements listed in Table XI. For $\bar{B} \rightarrow D^*\ell\bar{\nu}$, we combine the present results with two *BABAR* measurements of $\rho_{D^*}^2$ and $\mathcal{F}(1)|V_{cb}|$ [9,10] and four measurements of $\mathcal{B}(\bar{B} \rightarrow D^*\ell\bar{\nu})$ [6,9,10]. We neglect the tiny statistical correlations among the measurements and treat the systematic uncertainties as fully correlated within a given category (background, detector modeling, etc.). We assume the semileptonic decay widths of B^+ and B^0 to be equal and adjust all measurements to the values of the $Y(4S)$ and D decay branching fractions used in this article to obtain

$$\mathcal{B}(B^- \rightarrow D^{*0}\ell\bar{\nu}) = (5.49 \pm 0.19)\%, \quad (31)$$

$$\rho_{D^*}^2 = 1.20 \pm 0.04, \quad (32)$$

$$\mathcal{F}(1)|V_{cb}| = (34.8 \pm 0.8) \times 10^{-3}. \quad (33)$$

The associated χ^2 probabilities of the averages are 0.39, 0.86, and 0.27, respectively. The average of the $\mathcal{B}(\bar{B} \rightarrow D\ell\bar{\nu})$ result with the two existing *BABAR* measurements [6] is

$$\mathcal{B}(B^- \rightarrow D^0\ell\bar{\nu}) = (2.32 \pm 0.09)\% \quad (34)$$

with a χ^2 probability of 0.88.

The simultaneous measurements of $\mathcal{G}(1)|V_{cb}|$ and $\mathcal{F}(1)|V_{cb}|$ allow a determination of the ratio $\mathcal{G}(1)/\mathcal{F}(1)$

which can be compared directly with theory. We find

$$\text{Measured: } \mathcal{G}(1)/\mathcal{F}(1) = 1.20 \pm 0.09, \quad (35)$$

$$\text{Theory: } \mathcal{G}(1)/\mathcal{F}(1) = 1.17 \pm 0.04, \quad (36)$$

where we have assumed the theory errors on $\mathcal{F}(1)$ [33] and $\mathcal{G}(1)$ [31] to be independent. The measured ratio is consistent with the predicted ratio.

The excellent description obtained in this fit, at the 1% statistical level, of the dominant Cabibbo-favored semileptonic decays will facilitate the determination of decay rates of Cabibbo-suppressed decays over a larger kinematic region than has been feasible to date. This will result in a reduction in the theoretical uncertainty on the determination of $|V_{ub}|$.

To summarize, we use a global fit to $D^0\ell$ and $D^+\ell$ combinations to measure the form-factor parameters

$$\begin{aligned} \rho_D^2 &= 1.20 \pm 0.04 \pm 0.07, \\ \rho_{D^*}^2 &= 1.22 \pm 0.02 \pm 0.07, \end{aligned} \quad (37)$$

in the commonly used HQET-based parametrization [16], and the branching fractions

$$\begin{aligned} \mathcal{B}(B^- \rightarrow D^0\ell\bar{\nu}) &= (2.34 \pm 0.03 \pm 0.13)\%, \\ \mathcal{B}(B^- \rightarrow D^{*0}\ell\bar{\nu}) &= (5.40 \pm 0.02 \pm 0.21)\%, \end{aligned} \quad (38)$$

where the first error is statistical and the second systematic. The fit assumes the semileptonic decay widths of B^+ and B^0 to be equal. These results are consistent with previous *BABAR* measurements [6,9,10]. From these slopes and branching fractions we determine

$$\begin{aligned} \mathcal{G}(1)|V_{cb}| &= (43.1 \pm 0.8 \pm 2.3) \times 10^{-3}, \\ \mathcal{F}(1)|V_{cb}| &= (35.9 \pm 0.2 \pm 1.2) \times 10^{-3}. \end{aligned} \quad (39)$$

The $\mathcal{G}(1)|V_{cb}|$ value is twice as precise as the current world average. The precision on $\mathcal{F}(1)|V_{cb}|$ equals that of the best single measurement, while coming from a complementary technique. From these results, we extract two values for $|V_{cb}|$:

$$\begin{aligned} D^*\ell\nu: |V_{cb}| &= (38.6 \pm 0.2 \pm 1.3 \pm 1.0) \times 10^{-3}, \\ D\ell\nu: |V_{cb}| &= (39.9 \pm 0.8 \pm 2.2 \pm 0.9) \times 10^{-3}, \end{aligned} \quad (40)$$

TABLE XI. Previously published *BABAR* results [6,9,10].

Parameters	Reference [9]	Reference [10]	Reference [6]
$\rho_{D^*}^2$	$1.191 \pm 0.048 \pm 0.028$	$1.16 \pm 0.06 \pm 0.08$	
$\mathcal{B}(B^- \rightarrow D^{*0}\ell\bar{\nu})(\%)$		$5.56 \pm 0.08 \pm 0.41$	$5.83 \pm 0.15 \pm 0.30$
$\mathcal{B}(\bar{B}^0 \rightarrow D^{*+}\ell\bar{\nu})(\%)$	$4.69 \pm 0.04 \pm 0.34$		$5.49 \pm 0.16 \pm 0.25$
$\mathcal{F}(1) V_{cb} (\times 10^{-3})$	$34.4 \pm 0.3 \pm 1.1$	$35.9 \pm 0.6 \pm 1.4$	
$\mathcal{B}(B^- \rightarrow D^0\ell\bar{\nu})(\%)$			$2.33 \pm 0.09 \pm 0.09$
$\mathcal{B}(\bar{B}^0 \rightarrow D^+\ell\bar{\nu})(\%)$			$2.21 \pm 0.11 \pm 0.12$

where the errors correspond to statistical, systematic, and theoretical uncertainties, respectively.

ACKNOWLEDGMENTS

We are grateful for the extraordinary contributions of our PEP-II colleagues in achieving the excellent luminosity and machine conditions that have made this work possible. The success of this project also relies critically on the expertise and dedication of the computing organizations that support *BABAR*. The collaborating institutions wish to thank SLAC for its support and the kind hospitality extended to them. This work is supported by the U.S. Department of Energy and National Science Foundation, the Natural Sciences and Engineering Research Council (Canada), the Commissariat à l'Énergie Atomique and Institut National de Physique Nucléaire et de Physique des Particules (France), the Bundesministerium für Bildung und Forschung and Deutsche Forschungsgemeinschaft (Germany), the Istituto Nazionale di Fisica Nucleare (Italy), the Foundation for Fundamental Research on Matter (The Netherlands), the Research Council of Norway, the Ministry of Education and Science of the Russian Federation, Ministerio de Educación y Ciencia (Spain), and the Science and Technology Facilities Council (United Kingdom). Individuals have received support from the Marie-Curie IEF program (European Union) and the A. P. Sloan Foundation.

APPENDIX A: MODELING OF $\bar{B} \rightarrow D^{**} \ell \nu_\ell$ DECAYS

The differential decay rates of $\bar{B} \rightarrow D^{**} \ell \nu_\ell$ decays are given as functions of w and θ [23]. This θ is the angle between the charged lepton and the charmed meson in the rest frame of the virtual W boson. Thus θ is related to θ_ℓ , which is defined in Fig. 5, such that

$$\cos\theta = \cos(\pi - \theta_\ell) = -\cos\theta_\ell. \quad (\text{A1})$$

In the following subsections, we use the same notation as above, r and R , for the mass ratios of all four D^{**} mesons. However, it is implied that these are the ratios taken with corresponding charmed meson masses. The following notations are also used in the form-factor formulas in the following subsections:

$$\varepsilon_b \equiv \frac{1}{2m_b}, \quad \varepsilon_c \equiv \frac{1}{2m_c} \quad (\text{A2})$$

and

$$\begin{aligned} \bar{\Lambda} &= \text{energy of the ground state doublet } (D \text{ and } D^*), \\ \bar{\Lambda}' &= \text{energy of the excited } \frac{3}{2}^+ \text{ doublet } (D_1 \text{ and } D_2^*), \\ \bar{\Lambda}^* &= \text{energy of the excited } \frac{1}{2}^+ \text{ doublet } (D_0^* \text{ and } D_1'). \end{aligned} \quad (\text{A3})$$

1. $\bar{B} \rightarrow D_1 \ell \bar{\nu}$

The differential decay rate is given by

$$\frac{d^2\Gamma_{D_1}}{dw d\cos\theta} = \Gamma_z r^3 (w^2 - 1)^{1/2} I_{D_1}(w, \theta), \quad (\text{A4})$$

where $\Gamma_z \equiv \frac{G_F^2 |V_{cb}|^2 m_B^5}{64\pi^3}$ and

$$\begin{aligned} I_{D_1}(w, \theta) &= (1 - \cos^2\theta) \\ &\times [(w - r)f_{V_1} + (w^2 - 1)(f_{V_3} + rf_{V_2})]^2 \\ &+ (1 - 2rw + r^2) \\ &\times [(1 + \cos^2\theta)(f_{V_1}^2 + (w^2 - 1)f_A^2) \\ &- 4\cos\theta\sqrt{w^2 - 1}f_{V_1}f_A], \end{aligned} \quad (\text{A5})$$

and $f_{V_1}(w)$, $f_{V_2}(w)$, $f_{V_3}(w)$, and $f_A(w)$ are form factors which are given by

$$\begin{aligned} \sqrt{6}f_A &= -(w + 1)\tau - \varepsilon_b(w - 1) \\ &\times [(\bar{\Lambda}' + \bar{\Lambda})\tau - (2w + 1)\tau_1 - \tau_2] \\ &- \varepsilon_c[4(w\bar{\Lambda}' - \bar{\Lambda})\tau - 3(w - 1)(\tau_1 - \tau_2)], \\ \sqrt{6}f_{V_1} &= (1 - w^2)\tau - \varepsilon_b(w^2 - 1) \\ &\times [(\bar{\Lambda}' + \bar{\Lambda})\tau - (2w + 1)\tau_1 - \tau_2] \\ &- \varepsilon_c[4(w + 1)(w\bar{\Lambda}' - \bar{\Lambda})\tau \\ &- 3(w^2 - 1)(\tau_1 - \tau_2)], \\ \sqrt{6}f_{V_2} &= -3\tau - 3\varepsilon_b[(\bar{\Lambda}' + \bar{\Lambda})\tau - (2w + 1)\tau_1 - \tau_2] \\ &- \varepsilon_c[(4w - 1)\tau_1 + 5\tau_2], \\ \sqrt{6}f_{V_3} &= (w - 2)\tau + \varepsilon_b(2 + w) \\ &\times [(\bar{\Lambda}' + \bar{\Lambda})\tau - (2w + 1)\tau_1 - \tau_2] \\ &+ \varepsilon_c[4(w\bar{\Lambda}' - \bar{\Lambda})\tau + (2 + w)\tau_1 + (2 + 3w)\tau_2]. \end{aligned} \quad (\text{A6})$$

Here τ is the leading Isgur-Wise function, which is assumed to be a linear form [23],

$$\tau(w) = \tau(1)[1 + \hat{\tau}'(w - 1)]. \quad (\text{A7})$$

Uncertainty in the first order expansion of the Isgur-Wise function is parametrized in τ_1 and τ_2 . In approximation B₁ one sets

$$\tau_1 = 0, \quad \tau_2 = 0, \quad (\text{A8})$$

while in approximation B₂ one takes

$$\tau_1 = \bar{\Lambda}\tau, \quad \tau_2 = -\bar{\Lambda}'\tau. \quad (\text{A9})$$

2. $\bar{B} \rightarrow D_2^* \ell \bar{\nu}$

The differential decay rate is given by

$$\frac{d^2\Gamma_{D_2^*}}{dw d\cos\theta} = \Gamma_z r^3 (w^2 - 1)^{3/2} \frac{1}{2} J_{D_2^*}(w, \theta), \quad (\text{A10})$$

where

$$I_{D_2^*}(w, \theta) = \frac{4}{3}(1 - \cos^2\theta) \times [(w - r)k_{A_1} + (w^2 - 1)(k_{A_3} + rk_{A_2})]^2 + (1 - 2rw + r^2) \times [(1 + \cos^2\theta)(k_{A_1}^2 + (w^2 - 1)k_V^2) - 4\cos\theta\sqrt{w^2 - 1}k_{A_1}k_V] \quad (\text{A11})$$

and $k_V(w)$, $k_{A_1}(w)$, $k_{A_2}(w)$, and $k_{A_3}(w)$ are form factors which are given by

$$k_V = -\tau - \varepsilon_b[(\bar{\Lambda}' + \bar{\Lambda})\tau - (2w + 1)\tau_1 - \tau_2] - \varepsilon_c(\tau_1 - \tau_2), \quad (\text{A12})$$

$$k_{A_1} = -(1 + w)\tau - \varepsilon_b(w - 1) \times [(\bar{\Lambda}' + \bar{\Lambda})\tau - (2w + 1)\tau_1 - \tau_2] - \varepsilon_c(w - 1)(\tau_1 - \tau_2),$$

$$k_{A_2} = -2\varepsilon_c\tau_1k_{A_3} = \tau + \varepsilon_b[(\bar{\Lambda}' + \bar{\Lambda})\tau - (2w + 1)\tau_1 - \tau_2] - \varepsilon_c(\tau_1 + \tau_2).$$

3. $\bar{B} \rightarrow D_0^* \ell \bar{\nu}$

The differential decay rate is given by

$$\frac{d^2\Gamma_{D_0^*}}{dw d\cos\theta} = \Gamma_z r^3 (w^2 - 1)^{3/2} I_{D_0^*}(w, \theta), \quad (\text{A13})$$

where

$$I_{D_0^*}(w, \theta) = (1 - \cos^2\theta)[(1 + r)g_+ - (1 - r)g_-]^2 \quad (\text{A14})$$

and $g_+(w)$ and $g_-(w)$ are form factors which are given by

$$g_+ = \varepsilon_c \left[2(w - 1)\zeta_1 - 3\zeta \frac{w\bar{\Lambda}^* - \bar{\Lambda}}{w + 1} \right] - \varepsilon_b \left[\frac{\bar{\Lambda}^*(2w + 1) - \bar{\Lambda}(w + 2)}{w + 1} \zeta - 2(w - 1)\zeta_1 \right],$$

$$g_- = \zeta \quad (\text{A15})$$

with

$$\zeta(w) = \frac{w + 1}{\sqrt{3}} \tau(w). \quad (\text{A16})$$

In approximation B_1 one uses

$$\zeta_1 = 0, \quad \zeta_2 = 0, \quad (\text{A17})$$

while in approximation B_2 one takes

$$\zeta_1 = \bar{\Lambda}\zeta, \quad \zeta_2 = -\bar{\Lambda}^*\zeta. \quad (\text{A18})$$

4. $\bar{B} \rightarrow D_1' \ell \bar{\nu}$

The differential decay rate is given by

$$\frac{d^2\Gamma_{D_1'}}{dw d\cos\theta} = \Gamma_z r^3 (w^2 - 1)^{1/2} I_{D_1'}(w, \theta), \quad (\text{A19})$$

where

$$I_{D_1'}(w, \theta) = (1 - \cos^2\theta) \times [(w - r)g_{V_1} + (w^2 - 1)(g_{V_3} + rg_{V_2})]^2 + (1 - 2rw + r^2) \times [(1 + \cos^2\theta)(g_{V_1}^2 + (w^2 - 1)g_A^2) - 4\cos\theta\sqrt{w^2 - 1}g_{V_1}g_A], \quad (\text{A20})$$

and $g_{V_1}(w)$, $g_{V_2}(w)$, $g_{V_3}(w)$, and $g_A(w)$ are form factors which are given by

$$g_A = \zeta + \varepsilon_c \left[\frac{w\bar{\Lambda}^* - \bar{\Lambda}}{w + 1} \zeta \right] - \varepsilon_b \left[\frac{\bar{\Lambda}^*(2w + 1) - \bar{\Lambda}(w + 2)}{w + 1} \zeta - 2(w - 1)\zeta_1 \right],$$

$$g_{V_1} = (w - 1)\zeta + \varepsilon_c(w\bar{\Lambda}^* - \bar{\Lambda})\zeta - \varepsilon_b[(\bar{\Lambda}^*(2w + 1) - \bar{\Lambda}(w + 2))\zeta - 2(w^2 - 1)\zeta_1],$$

$$g_{V_2} = 2\varepsilon_c\zeta_1,$$

$$g_{V_3} = -\zeta - \varepsilon_c \left[\frac{w\bar{\Lambda}^* - \bar{\Lambda}}{w + 1} \zeta + 2\zeta_1 \right] + \varepsilon_b \left[\frac{\bar{\Lambda}^*(2w + 1) - \bar{\Lambda}(w + 2)}{w + 1} \zeta - 2(w - 1)\zeta_1 \right]. \quad (\text{A21})$$

- [1] N. Cabibbo, Phys. Rev. Lett. **10**, 531 (1963); M. Kobayashi and T. Maskawa, Prog. Theor. Phys. **49**, 652 (1973).
 [2] O. Buchmüller and H. Flächer, Phys. Rev. D **73**, 073008 (2006); C. Schwanda *et al.* (Belle Collaboration), Phys. Rev. D **78**, 032016 (2008).

- [3] D. Buskulic *et al.* (ALEPH Collaboration), Phys. Lett. B **395**, 373 (1997).
 [4] J. Bartelt *et al.* (CLEO Collaboration), Phys. Rev. Lett. **82**, 3746 (1999).
 [5] K. Abe *et al.* (Belle Collaboration), Phys. Lett. B **526**, 258 (2002).

- [6] B. Aubert *et al.* (BABAR Collaboration), Phys. Rev. Lett. **100**, 151802 (2008).
- [7] N. E. Adam *et al.* (CLEO Collaboration), Phys. Rev. D **67**, 032001 (2003).
- [8] K. Abe *et al.* (Belle Collaboration), Phys. Lett. B **526**, 247 (2002).
- [9] B. Aubert *et al.* (BABAR Collaboration), Phys. Rev. D **77**, 032002 (2008).
- [10] B. Aubert *et al.* (BABAR Collaboration), Phys. Rev. Lett. **100**, 231803 (2008).
- [11] Review of Particle Properties, C. Amsler *et al.*, Phys. Lett. B **667**, 1 (2008).
- [12] H. Albrecht *et al.* (ARGUS Collaboration), Z. Phys. C **60**, 11 (1993).
- [13] B. Aubert *et al.* (BABAR Collaboration), Nucl. Instrum. Methods Phys. Res., Sect. A **479**, 1 (2002).
- [14] D. J. Lange, Nucl. Instrum. Methods Phys. Res., Sect. A **462**, 152 (2001).
- [15] S. Agostinelli *et al.* (Geant 4 Collaboration), Nucl. Instrum. Methods Phys. Res., Sect. A **506**, 250 (2003).
- [16] I. Caprini, L. Lellouch, and M. Neubert, Nucl. Phys. **B530**, 153 (1998).
- [17] M. Neubert, Phys. Rep. **245**, 259 (1994).
- [18] D. Scora and N. Isgur, Phys. Rev. D **52**, 2783 (1995).
- [19] J. L. Goity and W. Roberts, Phys. Rev. D **51**, 3459 (1995).
- [20] B. Aubert *et al.* (BABAR Collaboration), Phys. Rev. D **75**, 072002 (2007).
- [21] G. C. Fox and S. Wolfram, Nucl. Phys. **B149**, 413 (1979); **B157**, 543(E) (1979).
- [22] W. D. Hulsbergen, Nucl. Instrum. Methods Phys. Res., Sect. A **552**, 566 (2005).
- [23] A. K. Leibovich, Z. Ligeti, I. W. Stewart, and M. B. Wise, Phys. Rev. Lett. **78**, 3995 (1997); Phys. Rev. D **57**, 308 (1998). The scheme “ B_1 ” is used in the nominal fit; the other scheme “ B_2 ” is used in assessing systematic errors.
- [24] J. G. Korner and G. A. Schuler, Phys. Lett. B **242**, 119 (1990).
- [25] Heavy Flavor Averaging Group (HFAG), <http://www.slac.stanford.edu/xorg/hfag/index.html>.
- [26] B. Aubert *et al.* (BABAR Collaboration), arXiv:0808.0333 [Phys. Rev. Lett. (to be published)].
- [27] B. Aubert *et al.* (BABAR Collaboration), arXiv:0808.0528 [Phys. Rev. Lett. (to be published)].
- [28] D. Liventsev *et al.* (Belle Collaboration), Phys. Rev. D **77**, 091503 (2008).
- [29] K. Abe *et al.* (Belle Collaboration), Phys. Rev. Lett. **94**, 221805 (2005).
- [30] E. Barberio and Z. Was, Comput. Phys. Commun. **79**, 291 (1994); E. Barberio, B. van Eijk, and Z. Was, Comput. Phys. Commun. **66**, 115 (1991).
- [31] M. Okamoto *et al.*, Nucl. Phys. B, Proc. Suppl. **140**, 461 (2005).
- [32] A. Sirlin, Nucl. Phys. **B196**, 83 (1982).
- [33] C. Bernard *et al.*, arXiv:0808.2519 [Phys. Rev. D (to be published)].